Finite-size evaporating droplets in weakly-compressible homogeneous shear turbulence

Nicol Scapin[1]†, **Federico Dalla Barba**[2], **Giandomenico Lupo**[1], **Marco Edoardo Rosti**[3], **Christophe Duwig**[4], **Luca Brandt**[1,5]

[1]Department of Engineering Mechanics, Royal Institute of Technology (KTH), Stockholm, Sweden,

[2]Department of Industrial Engineering & CISAS, University of Padova, Padova, Italy,

[3]Complex Fluids and Flows Unit, Okinawa Institute of Science and Technology Graduate University (OIST), 1919-1 Tancha, Onna-son, Okinawa 904-0495, Japan,

[4]Department of Chemical Engineering, Royal Institute of Technology (KTH), Stockholm, Sweden,

[5]Department of Energy and Process Engineering, Norwegian University of Science and Technology (NTNU), Trondheim, Norway

We perform interface-resolved simulations of finite-size evaporating droplets in weakly-compressible homogeneous shear turbulence (HST). The study is conducted by varying three dimensionless physical parameters: the initial gas temperature over the critical temperature $T_{g,0}/T_c$, the initial droplet diameter over the Kolmogorov scale d_0/η and the surface tension, i.e. the shear-based Weber number, $We_{\mathcal{S}}$.

For the smallest $We_{\mathcal{S}}$, we first discuss the impact on the evaporation rate of the three thermodynamic models employed to evaluate the gas thermophysical properties: a constant property model and two variable-properties approaches where either the gas density or all the gas properties are allowed to vary. Taking this last approach as reference, the model assuming constant gas properties and evaluated with the "1/3" rule, is shown to predict the evaporation rate better than the model where the only variable property is the gas density. Moreover, we observe that the well-known Frössling/Ranz-Marshall correlation underpredicts the Sherwood number at low temperatures, $T_{g,0}/T_c = 0.75$.

Next, we show that the ratio between the actual evaporation rate in turbulence and the one computed in stagnant condition is always much higher than one for weakly deformable droplets: it decreases with $T_{g,0}/T_c$ without approaching unity at the highest $T_{g,0}/T_c$ considered. This suggests an evaporation enhancement due to turbulence also in conditions typical of combustion applications.

Finally, we examine the overall evaporation rate and the local interfacial mass-flux at higher $We_{\mathcal{S}}$, showing a positive correlation between evaporation rate and interfacial curvature, especially at the lowest $T_{g,0}/T_c$.

Key words: finite-size, evaporating droplets, homogeneous shear turbulence, weakly-compressible simulations.

† Email address for correspondence: nicolos@mech.kth.se

1. Introduction

The understanding of droplets evaporation in turbulent flows is a crucial aspect in many different contexts, such as geophysics and spray combustion to name a few. In the first example, evaporation is central for the formation and evolution of clouds and, more in general, in many of the *grand challenges of environmental fluid mechanics* (Dauxois *et al.* 2021). In the second example, droplets evaporation is a precursor of combustion; ensuring that all the liquid vaporizes before chemical reactions occur is fundamental to minimize the pollutants formation and to maximize the efficiency of the entire process (Birouk & Gökalp 2006). More recently, evaporation in turbulence acquired a prominent role also in our understanding of the fluid dynamics aspects of the COVID-19 spreading (e.g., droplet generation due to exhalation and airborne dispersion) as described in Mittal *et al.* (2020); Balachandar *et al.* (2020); Bourouiba (2021). Therefore, several studies have been conducted to understand how the relative humidity affects evaporation and condensation (Rosti *et al.* 2020; Ng *et al.* 2021; Chong *et al.* 2021) as well as on the interaction between droplets and turbulent flows (Bourouiba 2020; Rosti *et al.* 2021) with the ultimate goal of improving the social distancing guidelines.

Historically, evaporating droplets in turbulence have been the subject of numerous and extensive experimental campaigns which have mainly focused on the flow topology inside the droplets (Wong & Lin 1992; Mandal & Bakshi 2012), on the interaction between droplet dispersion and vapor clouds structure (De Rivas & Villermaux 2016; Villermaux *et al.* 2017; Sahu *et al.* 2018) and on evaporation enhancement of super-Kolmogorov (i.e., finite-size) droplets (Marti *et al.* 2017; Verwey & Birouk 2018, 2020). On the computational side, the most common approach has been the point particle method (Kuerten 2016; Maxey 2017) for the studies of sub-Kolmogorov droplets in different flow configurations, i.e. forced homogeneous isotropic turbulence (Mashayek 1998*a*; Weiss *et al.* 2018), homogeneous shear turbulence (Mashayek 1998*b*; Weiss *et al.* 2020), turbulent channel flow (Russo *et al.* 2014; Bukhvostova *et al.* 2014) and turbulent jets (Reveillon & Demoulin 2007; Wang *et al.* 2021). The main limitation of this approach is represented by the inherent need of empirical closure equations to model the mass, momentum and energy coupling between the disperse and the continuous phase. This feature limits their rigorous applications only to sub-Kolmogorov droplets (Elghobashi 2019) and hinders the possibility to investigate directly aspects such as the reciprocal influence of nearby droplets (Lupo *et al.* 2020; Chong *et al.* 2021) or the evaporation enhancement due to turbulence (which typically occurs for droplets of the order of the Taylor length, Birouk & Gökalp 2006). Moreover, assessing the impact of droplets deformation on the evaporation rate as well as the local interfacial mass flux distribution over the droplet surface is not possible, unless further models are introduced. On the other hand, less work has been dedicated to numerical simulations of droplets larger than the Kolmogorov scale and the only few works available consider homogeneous isotropic turbulence (HIT). Specifically, in Albernaz *et al.* (2017) the authors studied by means of a hybrid Lattice Boltzmann method (LBM) the deformation and heat transfer of a single droplet with diameter between 25η and 40η, with η the Kolmogorov length. In this setup, however, little can be said about the mass transfer because evaporation and condensation compensate for a statistically constant droplet volume. Recently, Dodd *et al.* (2021) employed a geometric volume of fluid method to study the evaporation of droplets at different volume fractions ($0.01 \% \leqslant \alpha \leqslant 1 \%$) with an initial droplet diameter ranging between 4η and 17η in order to highlight the limitations of point particle closures for the calculation of the evaporation rate and the semi-empirical correlations of the Sherwood number in absence of mean flow and for non-isolated droplets.

The limited number of studies and the need of further understanding of such a complex process motivates us to further investigate finite-size evaporating droplets in homogeneous-shear turbulence. As noted in Kasbaoui *et al.* (2017), this configuration can be regarded as one of intermediate complexity between homogeneous isotropic and non-homogeneous flows and it represents a particularly convenient set-up for two reasons. First, it allows to study shear flows without the complications induced by the presence of the walls. Next, given the intrinsic production of turbulent kinetic energy by the mean shear, turbulence is self-sustained without any external forcing and the flow achieves a statistically stationary condition (SS-HST) (Pumir 1996; Sekimoto *et al.* 2016). The SS-HST has been recently considered in multiphase flows, e.g. in Rosti *et al.* (2019*b*) for emulsions and in Tanaka (2017); Yousefi *et al.* (2020) for turbulence modulation by rigid particles of different shapes. In both cases, the characteristic length of the disperse phase was chosen larger than the Kolmogorov scale.

In the current study we therefore consider finite-size evaporating droplets in SS-HST, assuming an incompressible liquid surrounded by a compressible gas phase at higher temperature. The initial size, ranging between 10.5η and 21.5η, is chosen to focus on evaporation enhancement by turbulence (Verwey & Birouk 2020) and to elucidate the effects of the interface deformation. This last aspect is less discussed in literature and, so far, the spherical assumption has been invoked to describe the droplet shape also in fully resolved simulations (Lupo *et al.* 2019, 2020). Given the large parameter space which characterizes evaporating flows, here we focus on changing the ratio between the droplet initial diameter and the Kolmogorov scale (d_0/η), the surface tension and the initial gas temperature. Moreover, in all cases, to study the isolated droplet behavior, we consider a small initial liquid volume fraction, $\alpha_0 = 0.14$ %, corresponding to five droplets. The resulting parametric study aims at addressing the following questions:

a. What is the level of approximation of the estimated evaporation rates when the gas thermophysical properties are assumed constant?

b. What are the effects on the evaporation rate and on the liquid temperature of the droplet size? Moreover, how does the ratio K/K_0 (actual evaporation rate in turbulence over the evaporation rate in stagnant condition) changes when increasing the gas temperature in conditions relevant for combustion applications?

c. How does the interface deformation affects the evaporation rate and does the local interfacial mass-flux correlates with changes in the droplet shape?

To investigate this complex phenomenon numerically, we propose a new volume of fluid method for evaporating flows in weakly compressible homogeneously sheared turbulence, extending the algorithm in Scapin *et al.* (2020). The tool addresses the two main issues arising when performing this kind of simulations with more realistic and challenging conditions. First, as already remarked in Kasbaoui *et al.* (2017), numerical simulations in HST are demanding even in single phase since the commonly employed multistep time-integration schemes (e.g., Adams-Bashforth and Runge-Kutta), if employed in their classical formulation, are weakly unstable and, therefore, not adequate for long-time simulations. Next, since the HST computational domain does not possess any outflow boundary, a rigorous description of the two-phase evaporating system requires a compressible formulation that allows the thermodynamic pressure to vary with the state variables. To address the first issue, we present a modified version of the Adams-Bashforth scheme which recovers the analytical solution of Kelvin modes in the limit of the rapid distorsion theory (RTD) (Maxey 1982) and, overall, ensures a stable integration over long times. The second issue is addressed by deriving and presenting a new mathematical formulation for evaporating flows with phase change in the low Mach limit (weakly-

compressible formulation) with a detailed numerical implementation. Differently from other approaches available in literature (Wang *et al.* 2019; Ni *et al.* 2021), this formulation relaxes the assumption of constant thermodynamic pressure and allows its dynamic variation according to the global expansion and contraction of the compressible gas phase, as well as, on the amount of mass-flux exchanged at the interface.

This paper is organized as follows. In § 2, we introduce the mathematical model employed to describe a two-phase evaporating system, adapted to the HST configuration. In § 3, the numerical algorithm is presented, with a note on an improved Adams-Bashforth scheme for HST simulations. The results, discussed in § 4, focuses on the role played by the specific thermodynamic model used to describe the weakly-compressible phase and the effects on the evaporation induced by the variation of the shear-based Reynolds number and the shear-based Weber number. Finally, the main findings and conclusions are summarized in § 5.

2. Governing equations

2.1. *Mathematical model for weakly-compressible evaporating flows*

We consider a system of two immiscible and Newtonian fluids: a single component liquid (phase 1) and an ideal mixture of an inert gas and vaporized liquid (phase 2). The two phases are bounded by an infinitesimally small interface, through which mass, momentum and energy are exchanged. The evaporation is driven by the partial pressure of the inert gas in phase 2. To represent this system, a phase indicator function H is defined at position $\mathbf{x}$ and time t to distinguish between the two phases:

$$H(\mathbf{x},t) = \begin{cases} 1 & \text{if } \mathbf{x} \in V_l, \\ 0 & \text{if } \mathbf{x} \in V_g; \end{cases} \tag{2.1}$$

where V_l and V_g are the domains pertaining to the liquid and gas phases, divided by a zero-thickness interface $\Gamma(t) = V_l \bigcap V_g$.

Hereinafter and unless otherwise state, we assume that the liquid is incompressible with constant properties, while the gas is compressible and its properties are allowed to vary with temperature, pressure and composition. Thus, given the possible variation of the density with the state variables, we consider compressibility, which in this work is treated within the low Mach approximation (Majda & Sethian 1985). This allows to filter acoustic effects, while still retaining potentially large density variations in the bulk region of the compressible phase. Under this assumption, the conservation equations for species, momentum, thermal energy and mass across the interface read

$$\rho \frac{D\mathbf{u}}{Dt} = -\nabla p + \frac{1}{Re}\nabla \cdot \tau + \frac{\mathbf{f}_\sigma}{We}, \tag{2.2}$$

$$\rho_g \frac{DY_l^v}{Dt} = \frac{1}{ReSc}\nabla \cdot (\rho_g D_{lg}\nabla Y_l^v), \tag{2.3}$$

$$\rho c_p \frac{DT}{Dt} = \frac{1}{RePr}\nabla \cdot (k\nabla T) + \left(\Pi_{p,1}\frac{dp_{th}}{dt} + \frac{\rho_g D_{lg}}{ReSc}\sum_{j=1}^{2}\nabla h_j \cdot \nabla Y_j\right)(1-H) \tag{2.4}$$

$$- \frac{(\dot{m}_\Gamma \delta_\Gamma)}{Ste},$$

$$\dot{m}_\Gamma = \frac{1}{ReSc}\frac{\rho_{g,\Gamma} D_{lg,\Gamma}}{1-Y_{l,\Gamma}^v}\nabla_\Gamma Y_l^v \cdot \mathbf{n}_\Gamma. \tag{2.5}$$

Here, $\mathbf{u}$ is the fluid velocity assumed to be continuous in the two phases, p is the hydrodynamic pressure, T the temperature, h the enthalpy (with $\nabla h = \nabla(c_p T)$), Y_l^v the mass fraction of the vaporized liquid in the inert gas and $\dot{m}_\Gamma$ is the interfacial mass flux. In (2.2), τ is the viscous stress tensor for compressible Newtonian flows and $\mathbf{f}_\sigma = \kappa_\Gamma \delta_\Gamma$ with κ_Γ the interfacial curvature. The generic thermophysical property ξ (density ρ, dynamic viscosity μ, thermal conductivity k or specific heat capacity c_p) is computed with an arithmetic average, i.e. $\xi = 1 + (\lambda_\xi - 1)H$ where $\lambda_\xi = \xi_l/\xi_{g,r}$. Since ξ_l is kept constant and uniform no further modeling is needed, while the generic gas property ξ_g is computed with appropriate equation of states. The gas density ρ_g is computed with the ideal gas law and the liquid diffusion coefficient with the Wilke-Lee correlation (Reid *et al.* 1987). More details on how the remaining gas thermophysical properties are evaluated are given in appendix A. Unless otherwise stated all the property ratios λ_ξ are computed with respect to the reference gas property $\xi_{g,r}$, taken as the initial value.

In equations (2.2), (2.3),(2.5) and (2.4), different dimensionless parameters appear. By introducing a reference velocity u_r and reference length l_r, we define the Reynolds number $Re = \rho_{g,r} u_r l_r / \mu_{g,r}$, the Weber number $We = \rho_{g,r} u_r l_r / \sigma$ with σ is the surface tension; $Sc = \mu_{g,r}/(\rho_{g,r} D_{lg,r})$ and $Pr = \mu_{g,r} c_{pg,r}/k_{g,r}$ are the Schmidt and the Prandlt number. Note that the temperature equation (2.4) requires the definition of the Stefan number $Ste = c_{pg,r} T_{g,0}/\Delta h_{lv}$ where $T_{g,0}$ is the initial gas temperature and Δh_{lv} is the latent heat and of the dimensionless group $\Pi_{p,1} = R_u/(c_{pg,r} M_g)$ where M_g is the molar mass of the gas phase and R_u the universal gas constant. To form a close set of equations, two additional equations are needed, one for the velocity divergence and one for the thermodynamic pressure p_{th}:

$$\nabla \cdot \mathbf{u} = f_\Gamma(\mathbf{x}_\Gamma, t) + \left[\frac{f_Y(\mathbf{x}, t) + f_T(\mathbf{x}, t)}{p_{th}} - \left(1 - \frac{\Pi_{p,1}}{c_p \overline{M}_{m,av}} \right) \frac{1}{p_{th}} \frac{dp_{th}}{dt} \right] (1 - H), \quad (2.6)$$

$$\frac{1}{p_{th}} \frac{dp_{th}}{dt} \int_{V_g} \left(1 - \frac{\Pi_{p,1}}{c_p \overline{M}_{m,av}} \right) dV_g = \int_V \left[f_\Gamma(\mathbf{x}_\Gamma, t) + \frac{f_T(\mathbf{x}, t) + f_Y(\mathbf{x}, t)}{p_{th}} (1 - H) \right] dV. \tag{2.7}$$

In equations (2.6) and (2.7), the functions $f_\Gamma(\mathbf{x}_\Gamma, t)$, $f_Y(\mathbf{x}, t)$ and $f_T(\mathbf{x}, t)$ represent the different contributions to the total velocity divergence from the phase change, (f_Γ) and the change of the gas density either due to composition (f_Y) or to temperature (f_T):

$$f_\Gamma(\mathbf{x}_\Gamma, t) = \dot{m}_\Gamma \left(\frac{1}{\rho_{g,\Gamma}} - \frac{1}{\lambda_\rho} \right) \delta_\Gamma, \tag{2.8a}$$

$$f_Y(\mathbf{x}, t) = \frac{1}{ReSc} \frac{\overline{M}_{m,av}}{\rho_g} \left(\frac{1}{\lambda_M} - 1 \right) \nabla \cdot (\rho_g D_{lg} \nabla Y_l^v), \tag{2.8b}$$

$$f_T(\mathbf{x}, t) = \frac{1}{Re} \frac{\Pi_{p,1}}{c_p \overline{M}_{m,av}} \left[\frac{1}{Pr} \nabla \cdot (k \nabla T) + \frac{\rho_g D_{lg}}{Sc} \sum_{j=1}^2 \nabla h_j \cdot \nabla Y_j \right], \tag{2.8c}$$

where $\lambda_M = M_l/M_g$ is the molar mass ratio. The complete derivation of equations (2.6), (2.7) and of relations (2.8) is provided in appendix B.

2.2. *Governing equations for the HST configuration*

Equations (2.2), (2.3), (2.5), (2.4), (2.6) and (2.7) are solved in a periodic box assuming an imposed uniform mean shear $\mathcal{S}$, as depicted in figure 1. In a shear-periodic domain, the streamwise x and spanwise y directions are periodic, whereas the so-called shear-periodic
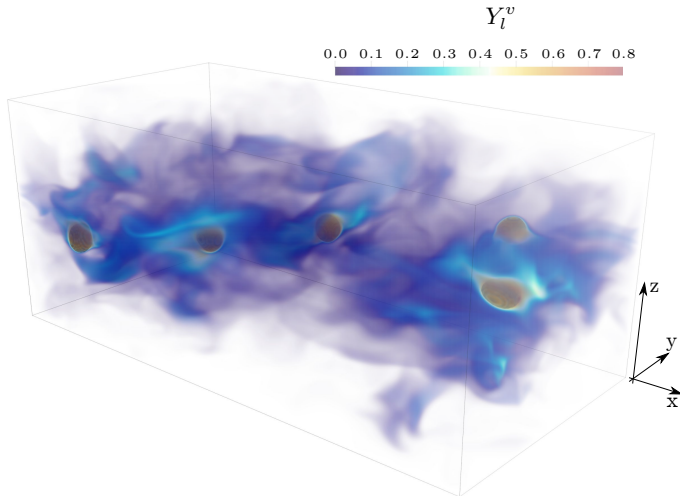
Scapin et. al.

$$Y_l^v$$

0.0 0.1 0.2 0.3 0.4 0.5 0.6 0.7 0.8

Figure 1: Sketch of the computational box: the rendering represents the volume contour of the vapor mass fraction for the case at $Re_{\mathcal{S}} = 6700$, $We_{\mathcal{S}} = 0.1$ and $T_{g,0}/T_c = 1.5$.

condition applies in the z direction, which reads for the generic scalar quantity g:

$$
\begin{aligned}
g(x + l_x, y, z) &= g(x, y, z), \\
g(x, y + l_y, z) &= g(x - \mathcal{S}t l_y, y, z), \\
g(x, y, z + l_z) &= g(x, y, z).
\end{aligned}
\tag{2.9}
$$

The presence of a mean velocity, i.e., $\mathcal{S}z$, suggests to decompose the velocity field $\mathbf{u}$ into a mean and a fluctuating component $\mathbf{u}'$,

$$
\mathbf{u} = \mathbf{u}' + \mathcal{S}z\mathbf{e}_x,
\tag{2.10}
$$

where $\mathbf{e}_x = (1, 0, 0)$. Given the decomposition (2.10), the momentum equation (2.2) is written in terms of $\mathbf{u}'$:

$$
\rho \left(\frac{D\mathbf{u}'}{Dt} + \mathcal{S}z\frac{\partial \mathbf{u}'}{\partial x} + \mathcal{S}w'\mathbf{e}_x \right) = -\nabla p + \frac{1}{Re_{\mathcal{S}}} \left[\nabla \cdot \tau + \mathcal{S} \left(\frac{\partial \mu}{\partial z}\mathbf{e}_x + \frac{\partial \mu}{\partial x}\mathbf{e}_z \right) \right] + \frac{\mathbf{f}_\sigma}{We_{\mathcal{S}}},
\tag{2.11}
$$

where $\mathbf{e}_z = (0, 0, 1)$. Three new terms appear: the first, $\mathcal{S}z\,(\partial \mathbf{u}'/\partial x)$, is the convection of the velocity-fluctuations by the mean shear. The second, $\mathcal{S}w'\mathbf{e}_x$, represents the production of streamwise momentum caused by the fluid parcel transport in the normal direction owing to the mean shear. The third and last term, $\mathcal{S}\,(\partial \mu/\partial z\mathbf{e}_x + \partial \mu/\partial x\mathbf{e}_z)$, represents the viscous dissipation due to the mean shear in the case of a fluid with variable viscosity. Note that $Re_{\mathcal{S}}$ and $We_{\mathcal{S}}$ are the shear-based Reynolds and the Weber numbers, computed taking $u_r = \mathcal{S}l_r$.

The same decomposition (2.10) is applied to the mass fraction and temperature equations, giving

$$
\rho_g \left(\frac{DY_l^v}{Dt} + \mathcal{S}z\frac{\partial Y_l^v}{\partial x} \right) = \frac{1}{Re_{\mathcal{S}}Sc} \nabla \cdot (\rho_g D_{lg} \nabla Y_l^v),
\tag{2.12}
$$

$$\rho c_p \left(\frac{DT}{Dt} + \mathcal{S}z\frac{\partial T}{\partial x} \right) = \frac{1}{Re_{\mathcal{S}}Pr} \nabla \cdot (k\nabla T) \tag{2.13}$$

$$+ \left(\Pi_{p,1}\frac{dp_{th}}{dt} + \frac{\rho_g D_{lg}}{Re_{\mathcal{S}}Sc} \sum_{j=1}^{2} \nabla h_j \cdot \nabla Y_j \right)(1-H) - \frac{\dot{m}_\Gamma \delta_\Gamma}{Ste}. \tag{2.14}$$

In equations (2.14) and (2.12), the two new terms, $\mathcal{S}z\,(\partial T/\partial x)$ and $\mathcal{S}z\,(\partial Y_l^v/\partial x)$, represent the convection of the temperature/vapor mass fraction by the mean shear.

3. Methodology

3.1. *Numerical method for low Mach HST simulations with phase change*

The governing equations are solved on a uniform Cartesian grid of equal spacing $\Delta x = \Delta y = \Delta z$, with a staggered arrangement for the velocity while the remaining scalar fields are defined at the cell centers. The convection terms of the governing equations are discretized with the QUICK scheme (Leonard 1979), while central schemes are employed for the diffusive terms. The numerical method for phase change in the incompressible limit is presented in (Scapin *et al.* 2020), while the details of the weakly-compressible two-phase code are reported in (Dalla Barba *et al.* 2020). Both implementations are based on the solver CaNS (Costa 2018), extended in this work to handle shear-periodic boundary conditions. In this section, we therefore only describe the main modifications needed to handle weakly-compressible phase-change processes in homogeneous shear turbulence (HST). The validation of the present algorithm against three benchmarks is provided in appendix C.

3.1.1. *Dispersed phase*

The first step is the interface reconstruction and subsequent advection, handled in a fully Eulerian manner using an algebraic volume of fluid (VoF) method, i.e., the MTHINC by Ii *et al.* (2012); Rosti *et al.* (2019*a*). We start from the topological equation for the phase indicator function (2.1):

$$\frac{\partial H}{\partial t} + \mathbf{u}_\Gamma \cdot \nabla H = 0, \tag{3.1}$$

where $\mathbf{u}_\Gamma$ is the interface velocity, taken as the sum of the extended liquid velocity $\mathbf{u}_l^{ext}$ and the contribution due to the interfacial mass flux $\dot{m}_\Gamma \mathbf{n}_\Gamma/\rho_l$, see Scapin *et al.* (2020) for more details. Note that since $\mathbf{u}_l^{ext}$ and $\mathbf{u}_\Gamma$ are derived from the one-fluid velocity $\mathbf{u}$, the decomposition (2.10) applies directly to the interface velocity.

Equation (3.1) is then re-written in terms of the the volume fraction, Φ, defined as the volumetric average of H over a discrete computation cell of volume $V_c = \Delta x \Delta y \Delta z$. Employing the decomposition (2.10) in the color function advection equation (3.1) yields

$$\frac{\partial \Phi}{\partial t} + \nabla \cdot (H^{ht}\mathbf{u}'_\Gamma) + \mathcal{S}z\frac{\partial H^{ht}}{\partial x} = \Phi\nabla \cdot \mathbf{u}'_\Gamma, \tag{3.2}$$

where H^{ht} represents the hyperbolic tangent function approximating the indicator function H. From equation (3.2), we see that an additional term is present, $\mathcal{S}z(\partial H^{ht}/\partial x)$, which represents the convection of volume fraction by $\mathcal{S}$.

Equation (3.2) is solved in three sub-steps. First, it is advanced by Δt^{n+1} to the new time step omitting the convection by the mean shear and the right hand side term. By employing the classical directional splitting, we obtain a provisional $\tilde{\Phi}$, see Ii *et al.* (2012)

for more details. Next, the convection by mean shear is included

$$\frac{\partial \tilde{\Phi}}{\partial t} + \mathcal{S} z \frac{\partial \tilde{H}^{ht}}{\partial x} = 0. \tag{3.3}$$

Note that the time derivative in equation (3.3) is computed explicitly for $\tilde{\Phi}$ while the convective term contains the phase indicator function H^{ht}. Since the latter is a function of the former and the mathematical form of this dependency varies according to the type of interface reconstruction method, it is possible to express the convective term as a function of Φ. Nevertheless, this would modify the advection velocity in (3.3) adding a spatial dependent term along the mean shear direction (i.e., x), making more elaborated and complex the application of the method of characteristics. For this reason, we prefer to compute this extra term by an additional directional splitting along x, with $\mathcal{S}z$ as advection velocity.

Finally, the divergence is corrected. This consists in adding, after the four directional splittings, a correction term proportional to the discrete velocity divergence:

$$\Phi^{n+1}_{i,j,k} = \tilde{\Phi}_{i,j,k} - \Delta t^{n+1} F^{n}_{i,j,k} + \Delta t^{n+1} \Phi^{n+1}_{i,j,k} (\nabla \cdot \mathbf{u}_\Gamma)^n_{i,j,k}, \tag{3.4}$$

where $\Phi^{n+1}_{i,j,k}$ is the volume fraction resulting from the directional splitting procedure, $F^{n}_{i,j,k}$ represents the correction used in the previous directional-splitting steps, and the last term is the volume correction which ensures that the interface velocity divergence is employed to update $\Phi^{n+1}_{i,j,k}$ (Scapin *et al.* 2020). The thermodynamic properties (ρ, μ, k and c_p) are then updated using the new value Φ^{n+1}.

3.1.2. *Vapor mass fraction equation*

The conservation of the vapor mass fraction, see equation (2.12), is solved only in the gas domain (i.e., V_g), assuming saturation conditions at the interface Γ. In other words, the value $Y^v_l = Y^v_{l,\Gamma}$, which is a function of the thermodynamic pressure and temperature, is imposed at the interface Γ as a Dirichlet boundary condition. To compute $Y^v_{l,\Gamma}$, we employ the Span-Wagner equation of state (see equations (A 6) and (A 7) in appendix A). Equation (2.12) is advanced with the first-Euler method neglecting the mean shear contribution. This yields a provisional vapor mass fraction field $\tilde{Y}^{n+1}_{v,l}$:

$$\rho^{n+1}_g \frac{\tilde{Y}^{v,n+1}_l - Y^{v,n}_l}{\Delta t^{n+1}} = -\rho^{n+1}_g (\mathbf{u} \cdot \nabla Y^v_l)^n + \frac{1}{Re_\mathcal{S} Sc} \nabla \cdot (\rho^{n+1}_g D^{n+1}_{lg} \nabla Y^{v,n}_l). \tag{3.5}$$

The calculation of the gradient in the convective part of (3.5) is performed as detailed in Scapin *et al.* (2020), while some modifications are required for the linear term as it contains the diffusion coefficient D_{lg} and the gas density ρ_g, which, in general, vary with the thermodynamic pressure, temperature and composition. Since the procedure can be performed dimension by dimension, we present the discretization along x as example, the same approach being repeated for the other two directions,

$$\frac{\partial}{\partial x}\left(\rho_g D_{lg} \frac{\partial Y^v_l}{\partial x}\right)_i = \frac{1}{\Delta x}\left((\rho_g D_{lg})_{i+1/2}\left.\frac{\partial Y^v_l}{\partial x}\right|_{i+1/2} - (\rho_g D_{lg})_{i-1/2}\left.\frac{\partial Y^v_l}{\partial x}\right|_{i-1/2}\right)_i. \tag{3.6}$$

The evaluation of the gradients $\partial Y^v_l / \partial x_{i\pm1/2}$ is performed on an irregular grid, employing one-sided finite difference equations for the cell cut from the interface or central scheme for cells away from the interface (see Scapin *et al.* 2020, for details). Next, the coefficients $(\rho_g D_{lg})_{i\pm1/2}$ are obtained as the arithmetic mean,

$$(\rho_g D_{lg})_{i\pm1/2} = 0.5[(\rho_g D_{lg})_i + (\rho_g D_{lg})^G]. \tag{3.7}$$

If the cell i and its neighbors $(i \pm 1)$ are not cut by the interface, $\rho_g D_{lg}^G$ is set equal to $(\rho_g D_{lg})_{i \pm 1}$. Otherwise, $(\rho_g D_{lg})^G$ is evaluated as:

$$(\rho_g D_{lg})^G = \frac{(\rho_g D_{lg})_\Gamma + (\theta - 1)(\rho_g D_{lg})_{i \pm 1}}{\theta}, \qquad (3.8)$$

where θ represents the sub-cell resolution computed from the level-set function, reconstructed from the volume of fluid field. Since eq. (3.8) poorly behaves for small values of θ, we set $(\rho_g D_{lg})^G = (\rho_g D_{lg})_i$ when $\theta \leqslant 1/4$. Note that equation (3.8) requires the value of the coefficient $(\rho_g D_{lg})$ at the interface location, i.e. $(\rho_g D_{lg})_\Gamma$. These are evaluated with the corresponding equations of state using the temperature and the vapor composition at the interface location. It is worth mentioning that we cannot access directly the liquid and gas temperature, separately, since the temperature equation is solved over the whole domain, irrespective of the interface location. Therefore, to avoid problems of artificial heating (especially when the difference between the gas and the liquid density is high) we locally reconstruct the gas temperature in V_l and the liquid temperature in V_g relying on a simple constant extrapolation of T. The resulting two fields, T_g and T_l, defined in few grid cells around the interface, are then used to update the thermophysical properties, see appendix A for more details.

Finally, the mean shear contribution is included using the method of characteristic over a time Δt^{n+1}:

$$\frac{\partial Y_l^v}{\partial t} + \mathcal{S} z \frac{\partial Y_l^v}{\partial x} = 0. \qquad (3.9)$$

Equation (3.9) can be conveniently re-written in more compact form as in Gerz *et al.* (1989); Kasbaoui *et al.* (2017):

$$Y_l^{v,n+1} = \tilde{Y}_l^{v,n+1}(\mathbf{x} - \Delta t^{n+1} \mathcal{S} z \mathbf{e}_x). \qquad (3.10)$$

Equation (3.10) is solved using a Fourier interpolation (Tanaka 2017), which ensures a spectral accuracy provided that Δt^{n+1} is chosen lower or equal than $(\mathcal{S} N_z)^{-1}$ where N_z is the number of grid points along the z direction (see section 3.2 for more details).

3.1.3. *Calculation of the interfacial mass-flux*

The interfacial mass-flux (2.5) is computed only in the gas region by projecting the interfacial gradient along the normal direction and adopting a dimension by dimension approach. The interfacial vapor mass fraction Y_l^v, gas density ρ_g and diffusion coefficient D_{lg} should be estimated at the interface location. Similarly to the case of the vapor mass fraction described in section 3.1.2, all these quantities depend on the local gas and liquid temperature and on the thermodynamic pressure. Therefore, we first estimate the interfacial liquid and gas temperature in those grid cells cut by the interface. Depending on the interface position, this is done in each direction independently, providing different estimates for the gas and liquid temperature for the three coordinates, $T_{p,\Gamma}^x$, $T_{p,\Gamma}^y$ and $T_{p,\Gamma}^z$ where the subscript p stands for the gas and liquid phase. The resulting values are averaged using the local normal, i.e.:

$$T_{p,\Gamma} = T_{p,\Gamma}^x n_x^2 + T_{p,\Gamma}^y n_y^2 + T_{p,\Gamma}^z n_z^2. \qquad (3.11)$$

Once $T_{p,\Gamma}$ is known, the values of $\rho_{g,\Gamma}$, $D_{lg,\Gamma}$ and $Y_{l,\Gamma}^v$ are computed using the corresponding equations of state, see appendix A. Note that by employing the procedure here explained, the mass flux $\dot{m}_\Gamma$ is available only on the grid nodes pertaining the gas region. Nevertheless, as equation (2.6) suggests, the values of $\dot{m}_\Gamma$ are needed also in some grid points inside the liquid region. Accordingly, $\dot{m}_\Gamma$ is extrapolated over a narrow band at the interface to populate all cells where $|\nabla \Phi|_{i,j,k} \neq 0$.

3.1.4. *Temperature equation*

The temperature equation (2.4) is solved using a whole domain approach as in Scapin *et al.* (2020), with additional care paid to the time discretization. The adopted approach follows the one proposed in Gerz *et al.* (1989) and has been improved here to enhance the numerical stability and to include the additional source terms due to the gas compressibility, phase change and enthalpy diffusion. First, a prediction temperature field $\tilde{T}$ is computed using the Adams-Bashforth method:

$$\frac{\tilde{T}^{n+1} - T^n}{\Delta t^{n+1}} = \left(1 + \frac{1}{2}\frac{\Delta t^{n+1}}{\Delta t^n}\right) RT^n - \left(\frac{1}{2}\frac{\Delta t^{n+1}}{\Delta t^n}\right) RT^{n-1}, \tag{3.12}$$

where the terms RT^n and RT^{n-1} include all the convective and diffusive terms at the current, n, and old time level, $n-1$. The term RT^{n-1} is first shear-mapped to the new time-level $n+1$ and this step has proved to be crucial for the numerical stability of the Adams-Bashforth scheme (see appendix D).

Next, the temperature field is shear-mapped to the new time-level $n+1$ by employing the same spectral interpolation described for the vapor mass fraction equation,

$$T^{n+1,*} = \tilde{T}(\mathbf{x} - \mathcal{S}z\Delta t^{n+1}\mathbf{e}_x). \tag{3.13}$$

Finally, the source terms in (2.4) are included using the first-order Euler scheme:

$$\rho^{n+1}c_p^{n+1}\frac{T^{n+1} - T^{n+1,*}}{\Delta t^{n+1}} = \Pi_{p,1}\left(\frac{dp_{th}}{dt}\right)^{ext}(1 - \Phi^{n+1}), \tag{3.14}$$

$$+ \frac{1}{Re_\mathcal{S}Sc}\left(\rho_g D_{lg}\sum_{j=1}^{2}\nabla Y_j \cdot \nabla h_j^*\right)^{n+1}(1 - \Phi^{n+1}),$$

$$- \frac{(\dot{m}_\Gamma |\nabla\Phi|)^{n+1}}{Ste},$$

where $(dp_{th}/dt)^{ext}$ represents the linear extrapolation in time of the derivative of the thermodynamic pressure. It is important to note that the second and third terms in equation (3.14), which include variables shear-mapped to the new time level, (i.e., Φ^{n+1} and $Y_{l,j}^{v,n+1}$) should be computed after (3.13).

3.1.5. *Thermal divergence and thermodynamic pressure*

The calculation of the velocity divergence is performed simply by discretizating the right-hand side of equation (2.6) node by node as done in Dalla Barba *et al.* (2020) for the case of weakly-compressible two-phase solvers without phase change. The calculation of the thermodynamic pressure requires, however, more care. In the low Mach framework, the role of p_{th} is to ensure mass conservation of the compressible phase at the discrete level, since it enters the calculation of the gas density. This cannot be fulfilled simply by the advection of the color-function, which is designed to satisfy the volume conservation of the incompressible liquid, or by the pressure-correction step through the imposition of the divergence constrain (2.6) on $\mathbf{u}$. In fact, these ensure only the overall volume conservation of the closed and isochoric system under consideration. Therefore, we compute p_{th} by integrating the equation for the gas density (equation A 1 in appendix A) over the computation domain occupied by the gas phase V_g (Demou *et al.* 2019; Dalla Barba

et al. 2020),

$$p_{th}^{n+1} = \frac{G_g^{n+1} \Pi_{p,2}}{\int_V \frac{\overline{M}_{m,av}^{n+1}}{T^{n+1}} (1 - \Phi^{n+1}) \, dx \, dy \, dz}. \tag{3.15}$$

The total mass of the gas G_g, used above, varies in time according to the following relation, derived from the material balance across the droplet surface,

$$\frac{dG_g}{dt} = \dot{m}_{t,\Gamma} = \int_V \dot{m}_\Gamma^{n+1} |\nabla \Phi^{n+1}| \, dx \, dy \, dz. \tag{3.16}$$

Once the volume integral in equation (3.16) is computed, the gas mass at the new time-level is computed from the time integration of (3.16):

$$G_g^{n+1} = G_g^n + \int_{t^n}^{t^{n+1}} \dot{m}_{t,\Gamma} \, dt. \tag{3.17}$$

To evaluate numerically the integral in (3.17), we employ a trapezoidal quadrature. With this approach, we impose correctly the conservation of the compressible phase at the discrete level.

3.1.6. *Momentum equation and pressure correction method*

Once the thermodynamic divergence is computed, the momentum equation (2.2) is solved with a standard pressure correction method, reported below in semi-discrete form:

$$\mathbf{RU}^{n-1} = \widetilde{\mathbf{RU}}^{n-1}(\mathbf{x} - \Delta t^n \mathcal{S} z \mathbf{e}_x), \tag{3.18}$$

$$\rho^{n+1} \left(\frac{\mathbf{u}^{\star\star} - \mathbf{u}^n}{\Delta t^{n+1}} \right) = \left(1 + \frac{1}{2} \frac{\Delta t^{n+1}}{\Delta t^n} \right) \mathbf{RU}^n - \left(\frac{1}{2} \frac{\Delta t^{n+1}}{\Delta t^n} \right) \mathbf{RU}^{n-1}, \tag{3.19}$$

$$\mathbf{u}^\star = \mathbf{u}^{\star\star}(\mathbf{x} - \Delta t^{n+1} \mathcal{S} z \mathbf{e}_x) + \frac{\Delta t^{n+1}}{\rho^{n+1}} \frac{\kappa_\Gamma^{n+1} \nabla \Phi^{n+1}}{We_{\mathcal{S}}}, \tag{3.20}$$

$$\nabla^2 p^{n+1} = \nabla \cdot \left[\left(1 - \frac{\rho_0^{n+1}}{\rho^{n+1}} \right) \nabla \hat{p} \right] + \frac{\rho_0^{n+1}}{\Delta t^{n+1}} \left(\nabla \cdot \mathbf{u}^\star - \nabla \cdot \mathbf{u}^{n+1} \right), \tag{3.21}$$

$$\mathbf{u}^{n+1} = \mathbf{u}^\star - \Delta t^{n+1} \left[\frac{1}{\rho_0^{n+1}} \nabla p^{n+1} + \left(\frac{1}{\rho^{n+1}} - \frac{1}{\rho_0^{n+1}} \right) \nabla \hat{p} \right], \tag{3.22}$$

where $\mathbf{RU}^n$ and $\mathbf{RU}^{n-1}$ in equation (3.19) include the convective and diffusive terms computed at the current and previous time level, neglecting the surface tension force and the mean shear contribution. As done for the temperature equation and explained in details in the appendix D, it is very important for the stability and the accuracy of the time integration scheme that the term $\mathbf{RU}^{n-1}$ is shear-mapped to the current time-level n. The intermediate velocity $\mathbf{u}^{\star\star}$ is shear-mapped to the new time-level $n+1$, similarly to what done for the temperature and vapor mass fraction, and updated with the contribution from the surface tension (Rosti *et al.* 2019*b*).

Finally, the pressure equation (3.21) is solved with a time-splitting technique which allows to transform the variable Poisson equation into a constant coefficient one (Dodd & Ferrante 2014). Note that ρ_0^{n+1} and $\hat{p}$ in (3.21) and (3.22) are the minimum density over the entire computational domain and the extrapolated hydrodynamic pressure $\hat{p} = (1 + (\Delta t^{n+1}/\Delta t^n))p^n - (\Delta t^{n+1}/\Delta t^n)p^{n-1}$. As already discussed in Motheau & Abraham (2016); Dalla Barba *et al.* (2020), the use of the pressure splitting to solve the variable density Poisson equation in a low-Mach framework is suitable when the temperature ratio between the two phases is below $2-3$, which is the case of the current study. Finally, it is

worth mentioning that the presence of the shear, if left untreated, would make the use of the eigenexpansion method to solve (3.21) not possible, since one direction is not periodic. For this reasons, in order to still benefit of the FFT-based solvers, equation (3.21) is solved in a coordinate system moving with the mean shear for which, triperiodic boundary conditions can be applied. The solution is then transformed back to the shear-periodic domain, as detailed in Tanaka (2017); Rosti *et al.* (2019*b*).

3.2. *Time-step restriction*

The time step Δt^{n+1} is estimated from the stability constraints of the overall system:

$$\Delta t^{n+1} = \min\left[C_{\Delta t_c}\Delta t_c^{n+1}, C_{\Delta t_d}\min\left(\Delta t_\mu, \Delta t_\sigma, \Delta t_m, \Delta t_k\right)^{n+1}, C_{\Delta t_{\mathcal{S}}}\frac{\Delta z}{\mathcal{S}l_z}\right], \qquad (3.23)$$

where Δt_c, Δt_σ, Δt_μ, Δt_m and Δt_k are the maximum allowable time steps due to convection, surface tension, momentum, thermal energy and mass diffusion. These can be determined as suggested in Scapin *et al.* (2020); Dalla Barba *et al.* (2020):

$$\Delta t_c = \frac{\Delta x}{|u_{\max}| + |v_{\max}| + |w_{\max}|}, \qquad\qquad \Delta t_\mu = \min\left(\min_{V_g}\left\{\frac{\mu_g}{\rho_g}\right\}, \frac{\lambda_\mu}{\lambda_\rho}\right)\frac{\Delta x^2 Re_{\mathcal{S}}}{6},$$

$$\Delta t_\sigma = \sqrt{\frac{We_{\mathcal{S}}(\min_{V_g}\{\rho_g\} + \lambda_\rho)\Delta x^3}{4\pi}}, \quad \Delta t_m = \min_{V_g}\{D_{lg}\}\frac{(\theta_m\Delta x)^2 Sc}{6},$$

$$\Delta t_k = \min\left(\min_{V_g}\left\{\frac{k_g}{\rho_g c_{pg}}\right\}, \frac{\lambda_k}{\lambda_\rho\lambda_{c_p}}\right)\frac{\Delta x^2 Pr}{6},$$

$$\tag{3.24}$$

where $|u_{i,\max}|$ is an estimate of the maximum value of the ith component of the flow velocity, $\theta_m = 0.25$ and $\max_{V_g}\{\xi_g\}$ and $\min_{V_g}\{\xi_g\}$ denote the maximum and minimum over the computational domain, V_g, of the generic thermophysical property of the gas phase. For the cases presented here, the convective contrain represents the main limitation; setting $C_{\Delta t_c} = 0.15$, $C_{\Delta t_d} = 0.5$ and $C_{\Delta t_{\mathcal{S}}} = 1$ was found sufficient for a stable and accurate time integration.

3.3. *Computational set-up*

Given the large number of dimensionless parameter that characterizes flows involving evaporation, we focus our attention on the role of the ratio between droplet initial diameter and the Kolmogorov dissipative flow scale (tuned by varying the shear-based Reynolds number, $Re_{\mathcal{S}}$), the role of surface tension (varying the shear-based Weber number $We_{\mathcal{S}}$), the ratio between the initial gas temperature and the critical temperature, $T_{g,0}/T_c$, and the type of model employed to evaluate the thermophysical properties of the gas phase during the simulations. Concerning this last aspect, we first consider all the gas thermophyisical properties constant and computed with a proper averaging between the liquid and the gas temperature (i.e., with the 1/3 rule by Hubbard *et al.* 1975) (case denoted as CP); secondly, we allow only the gas density ρ_g to vary (case denoted as VP$_\rho$) and, finally, we allow all the thermophysical properties to vary with the local thermodynamic variables and vapor composition (case VP$_a$). A summary of the numerical campaign is reported in table 1, together with the remaining dimensionless physical parameters, which are all kept constant. Note that the physical parameters reported in table 1 are representative of pentane evaporating droplets in dry air at high pressure (~ 43 bar). In particular, we will consider 3 values of the ratio $T_{g,0}/T_c = 0.75, 1.00, 1.50$ where T_c is the critical temperature (469.69 K for pentane), which gives $T_{g,0} = 354, 470$

Case	$T_{g,0}/T_c$	Model for ξ_g	$Re_{\mathcal{S}}$	$We_{\mathcal{S}}$	Da_v		Group	Definition	Value
1	1.50	CP	6700	0.02	0.8213		Pr	$\mu_{g,r}c_{pg,r}/k_{g,r}$	1.39
2	1.50	VP$_\rho$	6700	0.02	0.8213		Sc	$\mu_{g,r}/(\rho_{g,r}D_{lg,r})$	1.66
3	1.50	VP$_a$	6700	0.02	0.8213		Ste	$c_{pg,r}T_{g,r}/\Delta h_{lv}$	5.70
4	0.75	CP	6700	0.02	0.1528		λ_ρ	$\rho_l/\rho_{g,r}$	13.15
5	0.75	VP$_\rho$	6700	0.02	0.1528		λ_μ	$\mu_l/\mu_{g,r}$	2.10
6	0.75	VP$_a$	6700	0.02	0.1528		λ_{c_p}	$c_{pl}/c_{pg,r}$	2.00
7	1.00	VP$_a$	6700	0.02	0.5531		λ_k	$k_l/k_{g,r}$	1.87
8	1.50	VP$_a$	2800	0.02	0.9584		λ_M	M_l/M_g	2.58
9	1.00	VP$_a$	2800	0.02	0.6589		$\Pi_{p,1}$	$R_u/(M_g c_{pg,r})$	0.18
10	0.75	VP$_a$	2800	0.02	0.2341		$\Pi_{p,2}$	$p_{th,r}M_g/(\rho_{g,r}R_u T_{g,r})$	1.00
11	1.50	VP$_a$	6700	0.06	0.8212		$\Pi_{p,3}$	$p_c/p_{th,r}$	0.83
12	1.50	VP$_a$	6700	0.10	0.8213		α_0 [%]	$V_{l,0}/(l_x l_y l_z)$	0.14
13	0.75	VP$_a$	6700	0.06	0.1528		$N_{dp,0}$	−	5
14	0.75	VP$_a$	6700	0.10	0.1528		RH_0 [%]	−	0.0

Table 1: Left: Dimensionless parameters defining the investigated cases, the initial gas temperature over the critical temperature $T_{g,0}/T_c$, the thermodynamic model employed to evaluate the gas thermophysical property, the shear-based Reynolds number $Re_{\mathcal{S}} = \rho_{g,r}\mathcal{S}l_y^2/\mu_{g,r}$, and the shear-based Weber number $We_{\mathcal{S}} = \rho_{g,r}\mathcal{S}^2 d_0^3/\sigma$ with d_0 the initial droplet diameter. The vaporization Damköhler number, the ratio between the turbulence time scale and the evaporation time scale in stagnant conditions, $Da_v = \tau_t/\tau_{v,L}$, is also reported (see equation 4.4). Note that in the current study $d_0/l_y = 0.10$. Right: dimensionless parameters kept constant in the current study ($N_{dp,0}$ is the initial number of droplet, α_0 is the initial liquid volume and RH_0 is the initial relative humidity).

and 705 K. The initial liquid temperature $T_{l,0}$ is the wet bulb temperature at $T_{g,0}$ and corresponds to $T_{l,0} = 334, 388$ and 432 K.

The focus of the study is the behavior of evaporating isolated droplets in homogeneous shear turbulence and, therefore, we consider five isolated droplets (i.e., initial volume fraction $\alpha_0 \approx 0.14$ % with $N_{dp,0} = 5$), injected in a single-phase statistically steady-state HST field at the desired shear-based $Re_{\mathcal{S}}$ (2800 or 6700). For all the cases, the computational domain has the streamwise aspect ratio, $\mathcal{AR}_{xy} = l_x/l_y \approx 2.10$, and the cross-stream ratio, $\mathcal{AR}_{zy} = l_z/l_y \approx 1.05$. As discussed in Sekimoto *et al.* (2016), employing such values, the effects on the flow induced by a finite-size computational box are reduced. The domain is discretized with $1280 \times 608 \times 640$ grid points, thus ensuring not only an adequate resolution of the flow field (i.e., $\Delta x/\eta \approx 0.33$ for $Re_{\mathcal{S}} = 2800$ and $\Delta x/\eta \approx 0.40$ for $Re_{\mathcal{S}} = 6700$ where η is the Kolmogorov length-scale), but also of the droplets, whose initial resolution is 64 points per diameter. This value is consistent with our previous study (Scapin *et al.* 2020), where we have assessed that a minimum of 50 grid-points per diameter is needed to fully resolve mass, momentum and energy transfer across the droplet interface. Note that the resolution is also sufficient to resolve the smallest scales of the two active scalar fields, Y_l^v and T, since the associated Batchelor scales $\eta_{B,Y} = \eta/\sqrt{Sc}$ and $\eta_{B,T} = \eta/\sqrt{Pr}$, although smaller than the Kolmogorov scale, are always larger than Δx.

4. Results

4.1. *Comparison of the three thermodynamic models*

We start our analysis by assessing the influence on the evaporation dynamics of the type of thermodynamic model employed to evaluate the gas thermophysical properties. A common approach (Abramzon & Sirignano 1989; Lupo *et al.* 2019, 2020) is to consider the thermophysical properties of the gas phase uniform, constant and evaluate them at an intermediate temperature, $T_m = T_{g,0} + m(T_{g,0} - T_{l,0})$. Hubbard *et al.* (1975) show that the value $m = 1/3$ guarantees a good agreement between experimental results and the theoretical predictions based on the d^2–law (Langmuir 1918). In the mathematical framework introduced above, this amounts to limiting the expansion and contraction at the interface, i.e. the terms f_Y and f_T in (2.6), (2.7) become zero. Here, we will denote the results obtained with these assumptions as CP. In many fully-resolved simulations, the only thermophysical property allowed to vary is the density and this is typically done within the Oberbeck-Boussinesq approximation (Piedra *et al.* 2015). This model, denoted VP_ρ, is considered here to asses whether it can provide accurate results. In typical conditions of evaporating droplets, however, other thermophysical properties may play a role. In particular, ρ_g and D_{lg} scale differently with the gas temperature, i.e., $\rho_g \sim p_{th}/T_g$ and $D_{lg} \sim T_g^{1.5}/p_{th}$ and both appear in the expression of the interfacial mass flux. These variations may significantly affect the evaporation dynamics, especially when the difference between the liquid and the gas temperatures is large. We will therefore also consider variations of all the thermophysical properties, case VP_a. To compare the different models we consider two temperature ratios, $T_{g,0}/T_c = 0.75$ and $T_{g,0}/T_c = 1.50$ at $Re_\mathcal{S} = 6700$ and the lowest Weber number under consideration in this study, $We_\mathcal{S} = 0.02$, to limit droplet break-up and reduce the droplet deformation. Unless otherwise stated, the results refer to the averaged values over the five droplets initially in the computational domain and error bars are included to represent the droplet with the largest positive and negative deviation from the mean value. Firstly, we show the square of the normalized droplet diameter, see figure 2. From the cases at $T_{g,0}/T_c = 1.50$, we observe that the complete model and the constant property model provide similar evaporation rates; when the gas density is the only varying thermophysical property, the evaporation rate is the highest. This behavior can be attributed to the presence of colder gas around the droplets, leading to larger local gas densities (up to three times the initial gas density, see figure 3) and, thus, to increased evaporation rates, as shown in figure 4a where we report the time history of the surface-averaged gas temperature. Relaxing the assumption of constant liquid diffusion coefficient reduces $D_{lg} \propto T_g^{1.5}$. This counteracts the effect of the higher gas density, decreasing the overall evaporation rate, which approaches the values obtained assuming constant property values. The results at $T_{g,0}/T_c = 0.75$ show a limited impact of compressibility on the evaporation dynamics, with an almost identical evaporation from the CP and VP_a models. Once more, allowing only the gas density to vary leads to an overestimation of the evaporation rate, which is explained by a lower gas temperature and higher density at the interface, see figure 4b.   Note that in all the cases and regardless of the model, the mean evaporation rate represents a good estimation of the evaporation rate of the single droplet since the magnitude of the largest positive and the negative deviations (represented by the error bars in figure 2) is within 5 %.

Figure 5 displays the time evolution of the ratio between the instantaneous area $A = |\nabla\Phi|\Delta x^3$ and the area of a spherical droplet with same volume with error bars indicating the maximum and minimum values at each instance at $T_{g,0}/T_c = 1.5$ and $T_{g,0}/T_c = 0.75$. Note that the mean deviation form the spherical shape is always below 10 % (over the simulated physical time) which makes the present data suitable for comparisons with
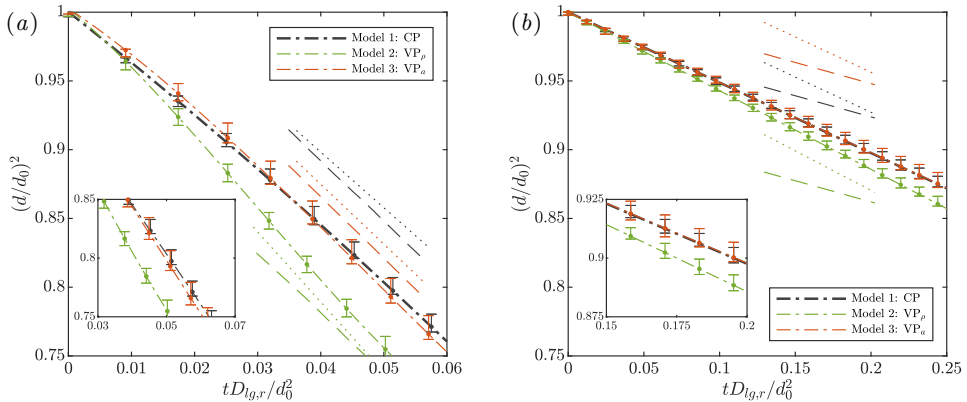
Figure 2: Normalized square droplet diameter, $(d/d_0)^2$, as a function of the dimensionless time (based on the diffusion time-scale) for temperature ratio (*a*) $T_{g,0}/T_c = 1.50$ and (*b*) $T_{g,0}/T_c = 0.75$ for $Re_{\mathcal{S}} = 6700$ and $We_{\mathcal{S}} = 0.02$. The *dotted curves* indicate the slope of the curves after the initial transient (extracted from the DNS), whereas the *dashed curves* is the estimation from the theoretical Frössling/Ranz-Marshall correlation. The length of the error bars indicates the droplet with the fastest/slowest evaporation rate among the five droplets in the simulations.
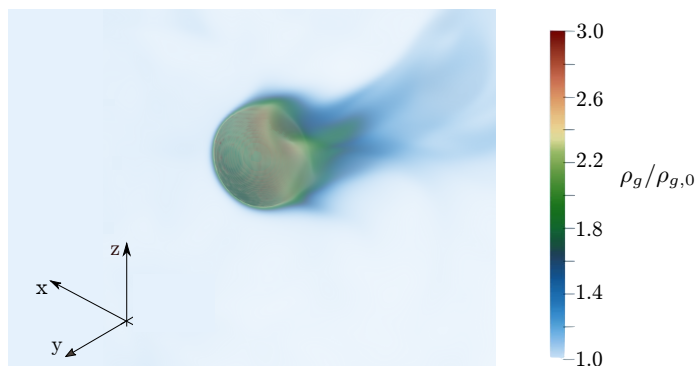
Figure 3: Volume rendering of the normalized gas density $\rho_g/\rho_{g,0}$ around a droplet for the case $Re_{\mathcal{S}} = 6700$, $We_{\mathcal{S}} = 0.02$ and $T_{g,0}/T_c = 1.5$.

existing scaling laws, which are commonly derived under the assumption of rigid and spherical droplets.

In all cases, the evaporation rate follows the linear trend predicted by the d^2–law since the droplets are isolated. We therefore test the closure relations available in literature against the data from the interface resolved simulations. To this end, we estimate the evaporation rate as proposed in Birouk & Gökalp (2006). First, we obtain the dimensionless evaporation rate in laminar conditions K_L (Abramzon & Sirignano 1989) as:

$$K_L = \frac{4\ Sh_{RM}}{Re_{\mathcal{S}} Sc} \frac{\log(1 + B_M)}{\lambda_\rho}, \tag{4.1}$$

where the Spalding number $B_M = (\langle Y_{l,\Gamma}^v \rangle_\Gamma - Y_{l,\infty}^v)/(1 - \langle Y_{l,\Gamma}^v \rangle_\Gamma)$ with $\langle \rangle_\Gamma$ the average over the surface Γ. The Sherwood number in equation (4.1) is estimated with the
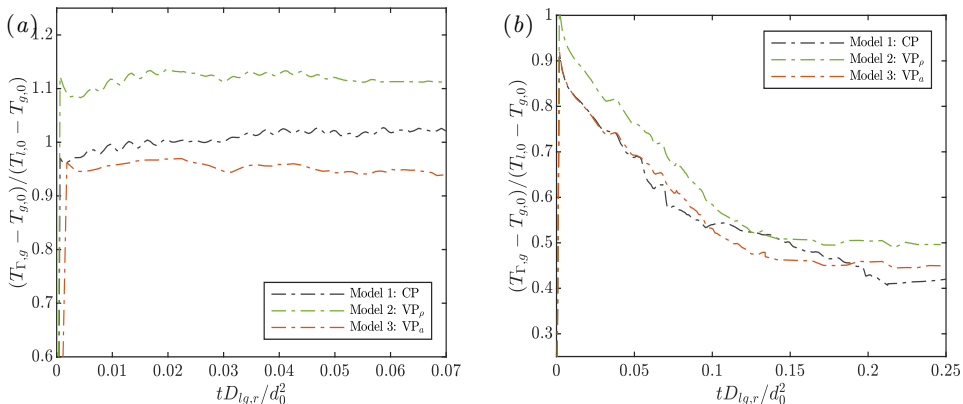
Figure 4: Normalized gas temperature at the interface as a function of the dimensionless time (based on the diffusion time-scale) for temperature ratio (*a*) $T_{g,0}/T_c = 1.50$ and (*b*) $T_{g,0}/T_c = 0.75$ for $Re_{\mathcal{S}} = 6700$ and $We_{\mathcal{S}} = 0.02$. $T_{g,0}$ and $T_{l,0}$ are the initial gas and liquid temperature.
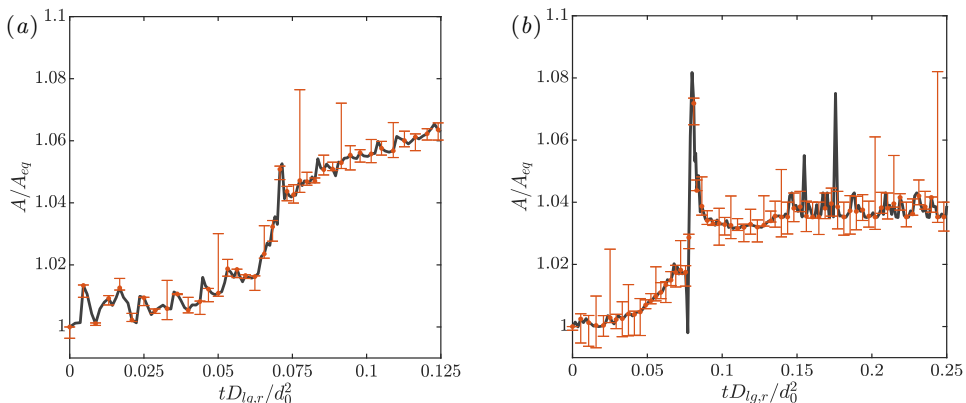

Figure 5: Ratio between the instantaneous interfacial area A and the area of a spherical droplet with same volume V, i.e., $A_{eq} = \pi^{1/3}(6V)^{2/3}$, for $We_{\mathcal{S}} = 0.02$ and a): $T_{g,0}/T_c = 1.50$ and b): $T_{g,0}/T_c = 0.75$. The upper lengths of the error bar refer to the droplet with the largest A/A_{eq}, while the lower lengths displacement to the droplet with lowest A/A_{eq}. The data refers to the simulations conducted with the VP_a thermodynamic models (negligible difference has been observed between the CP and the VP_a model).

Frössling/Ranz-Marshall correlation (Ranz *et al.* 1952; Birouk & Gökalp 2006),

$$Sh_{RM} = 2 + \frac{B_M}{(1+B_M)^{0.7}\log(1+B_M)}Sh_{0,RM}, \qquad (4.2)$$

with $Sh_{0,RM} = 2 + 0.552Re_d^{0.50}Sc^{0.33}$. In this last expression, Sc is the Schmidt number and Re_d is the droplet Reynolds number, defined as $Re_d = \rho_{g,r}|\mathbf{u}'_{l,d} - \mathbf{u}'_{g,d}|d/\mu_{g,r}$. Following the original reference (Ranz *et al.* 1952) and more recent works (Wang *et al.* 2021; Ng *et al.* 2021), we compute Re_d using the instantaneous droplet diameter, the instantaneous droplet velocity $\mathbf{u}'_{l,d}$ and the surrounding gas velocity $\mathbf{u}'_{g,d}$ at the droplet location (Ng *et al.* 2021). Note that this correlation is based on experiments with droplets larger than the Kolmogorov scale and in presence of a mean velocity field and, is therefore,

suitable for the current study. Finally, we correct equation (4.1) for the presence of turbulence via a Damköhler number (Gökalp *et al.* 1992):

$$\frac{K}{K_L} = 0.74 Da_v^{-0.115}. \tag{4.3}$$

In the above,

$$Da_v = \frac{\tau_t}{\tau_{v,L}}, \tag{4.4}$$

where $\tau_t = d_0^{2/3}/\langle\varepsilon_g\rangle_{M_g}^{1/3}$ is the characteristic time scale of the turbulent eddies, d_0 is the initial droplet diameter and $\langle\varepsilon_g\rangle_{M_g}$ is the mass averaged turbulent dissipation (see Abramzon & Sirignano 1989; Birouk & Gökalp 2006). The characteristic time scale of evaporation $\tau_{v,L}$, is computed as:

$$\tau_{v,L} = \frac{\delta_M}{V_r}, \tag{4.5}$$

where $\delta_M = d_0/(Sh_{RM} - 2)$ (Abramzon & Sirignano 1989) is the vapor film boundary layer thickness and V_r is the Stefan flow velocity computed as $V_r = 8\pi D_{lg,r} \log(1 + B_M)/d_0$. Note that while equations (4.1), (4.2) and the expressions for τ_t and δ_M are evaluated using also the instantaneous data from the interface-resolved simulations, the Stefan velocity V_r is evaluated a-priori as it depends only on the initial thermodynamic conditions.

The estimated values of K, dashed lines in figure 2, display a good agreement with the interface-resolved simulations at $T_{g,0}/T_c = 1.50$, especially for the CP and VP_a models, while a significant deviation is observed at $T_{g,0}/T_c = 0.75$, regardless of the thermodynamic model employed. Finally, it is worth noticing that the evaporation rate estimated with equation (4.1) depends linearly on Sh, whose calculation is generally affected by a higher degree of uncertainty (Lupo & Duwig 2020).

Next, we examine the temporal evolution of the Sherwood number, Sh, for the three different models, see figure 6, using directly the definition:

$$Sh = \frac{\dot{m}_{t,\Gamma} d_{eq}}{\rho_{g,r} D_{lg,r} A(\langle Y_{l,\Gamma}^v\rangle_\Gamma - Y_{l,\infty}^v)}. \tag{4.6}$$

Here $\dot{m}_{t,\Gamma}$ is the total interfacial mass flux, A the interfacial area, d_{eq} the instantaneous equivalent diameter (i.e., $d_{eq} = (6V/\pi)^3$), $\rho_{g,r}$ and $D_{lg,r}$ the reference gas density and gas-vapor diffusion coefficients, $\langle Y_{l,\Gamma}^v\rangle_\Gamma$ the surface-averaged vapor mass fraction at the interface and $Y_{l,\infty}^v$ the reference vapor mass fraction, i.e. its initial value. The Sherwood number defines the ratio between the mass transfer in the actual flow and the mass transfer by diffusion, i.e. evaporation in stagnant conditions, so that it can be used to quantify the effect of the flow on the evaporation. Note that since we perform a comparison among different thermodynamic models, the gas thermophysical properties in equation (4.6) are taken equal to the reference ones (i.e., the ones obtained with the "1/3" rule for the CP model, the ones at the initial condition for VP_a and VP_ρ models).

Both at high and low temperatures, Sh approaches an asymptotic value after the initial transient. Note that for the cases at $T_{g,0}/T_c = 1.5$, the transient is faster ($\Delta t D_{lg,r}/d_0^2 \approx 0.02$) than for the cases at $T_{g,0}/T_c = 0.75$ ($\Delta t D_{lg,r}/d_0^2 \approx 0.1$) since large temperature differences increase the evaporation rates. For the high-temperature cases, the Sh number differs significantly with the model employed, with the model VP_ρ giving the largest value of Sh for the reasons explained above. Conversely, at lower temperature, the three models provide a similar Sh, confirming the limited impact on the evaporation rate
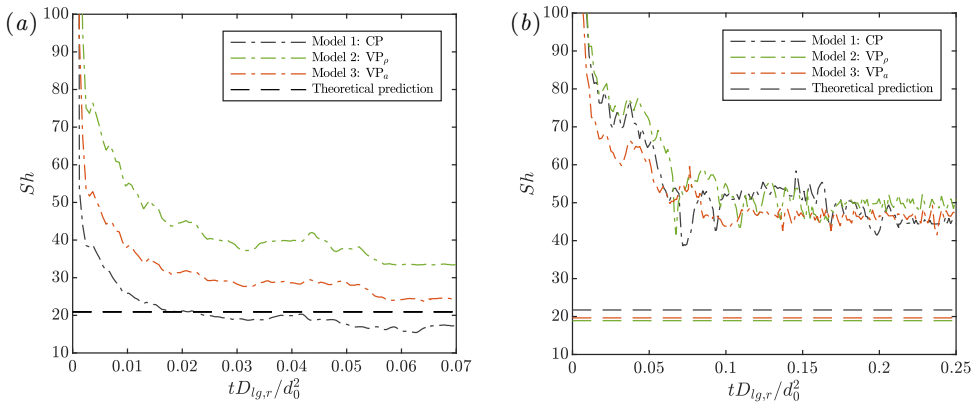
Figure 6: Temporal evolution of the Sherwood number as a function of the dimensionless time (based on the diffusion time scale) for temperature ratio (a) $T_{g,0}/T_c = 1.50$ and (b) $T_{g,0}/T_c = 0.75$ and $Re_{\mathcal{S}} = 6700$ and $We_{\mathcal{S}} = 0.02$. The dashed curves are the theoretical prediction provided from the a-priori analysis based on the Frössling/Ranz-Marshall correlation. For the cases at $T_{g,0}/T_c = 1.50$, only one value of Sh is reported as the three models provide almost identical predictions.

of the choice of the thermodynamic models in this regime. All other parameters being fixed, the Sherwood number is higher at the lower temperature ratio, $T_{g,0}/T_c = 0.75$ than for $T_{g,0}/T_c = 1.50$, regardless of the thermodynamic model used. Recalling that the Sherwood number is the ratio between the actual mass transfer and the mass transfer by diffusion, the increase of evaporation rate due to the background turbulence is thus larger at low temperatures. For the highest temperature ratio, the enhancement induced by the turbulence is lower since evaporation is mainly driven by the large temperature difference and by the larger values of $(\langle Y_{l,\Gamma}^v \rangle_\Gamma - Y_{l,\infty}^v)$.

As a final remark, note that the Sherwood number from the DNS agrees well with the estimation from the Frössling/Ranz-Marshall correlation at high temperature (cf. models CP and VP_a against the dashed line the figure 6). Conversely, at lower temperature, the estimated value is much lower than the one extracted from the direct numerical simulations, indicating that the Frössling/Ranz-Marshall correlation underpredicts convective effects due to turbulence at low evaporation rates, i.e. when the evaporation time becomes longer than the turbulence time scale ($Da_v \lesssim 0.2$ instead of $Da_v \approx 1$ as shown in table 1). This finding is consistent with the recent investigations in HIT performed by Méès *et al.* (2020) and suggests the need of including the turbulent effects (via the vaporization Damköhler number) in the available correlations for the Sherwood number and more in general in the evaporation models (Lupo *et al.* 2020).

4.2. *Effects of the shear-based Reynolds number*

We now consider the effect of the shear-based Reynolds number on the evaporation rate. Reducing from $Re_{\mathcal{S}} = 6700$ to $Re_{\mathcal{S}} = 2800$ results in a reduction of the ratio between the initial droplet diameter and the Kolmogorov length scale from $d_0/\eta = 21.5$ to $d_0/\eta = 10.5$. For this analysis, we assume $We_{\mathcal{S}} = 0.02$, three temperature ratios, $T_{g,0}/T_c = 0.75 - 1.00 - 1.50$ and employ the complete model (i.e., VP_a). We first examine the reduction of the droplet diameter, $(d/d_0)^2$, as a function of the diffusion time-scale $tD_{lg,r}/d_0^2$, see figure 7a. In all cases, droplets with larger d_0/η (i.e. higher $Re_{\mathcal{S}}$) evaporate faster, in agreement with previous experimental studies in homogeneous isotropic turbulence
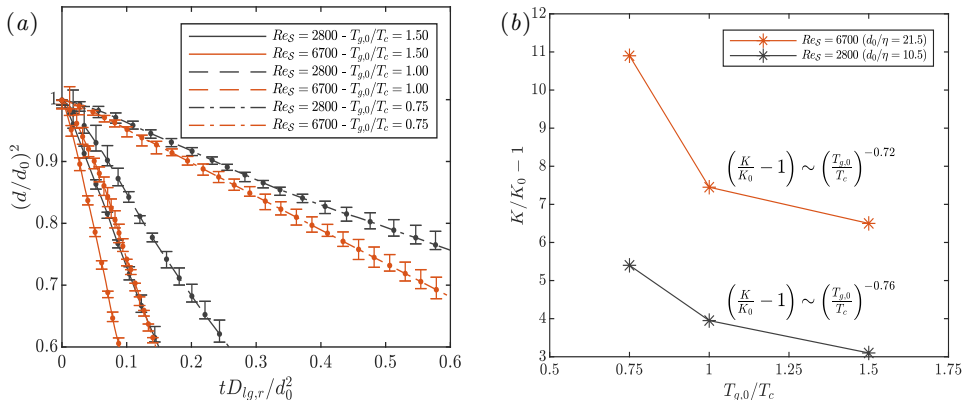
Figure 7: a) Normalized square droplet diameter $(d/d_0)^2$ as a function of the diffusion time-scale tD_{lg}/d_0^2. b) Ratio between the turbulent evaporation rate K and the one at stagnant conditions, $K_0 = (8/\lambda_\rho)\log(1 + B_M)$ with $B_M = (Y_{l,\Gamma}^v - Y_{l,\infty}^v)/(1 - Y_{l,\Gamma}^v)$. The data refer to the cases at $Re_{\mathcal{S}} = 2800 - 6700$ and $T_{g,0}/T_c = 1.5, 1.00$ and 0.75. The length of the error bars indicates the droplet with the fastest/slowest evaporation rate among the five droplets in the simulations.

(Verwey & Birouk 2018, 2020) and in the presence of a mean flow (Marti *et al.* 2017). This is explained by the enhanced surface vapor gradient and faster dispersion of the vapor around the droplet for larger d_0/η, related to the fact that larger flow structures are more energetic. Note that a relative increase of the evaporation rate, quantified as the ratio between the evaporation rate K extracted from the DNS and the one computed in stagnant conditions, K_0, occurs at all temperatures as reported in figure 7b and it scales with the dimensionless gas temperature with similar exponents for the two different d_0/η investigated, i.e. $(T_{g,0}/T_c)^{-0.76}$ for $d_0/\eta = 21.5$ and $(T_{g,0}/T_c)^{-0.72}$ for $d_0/\eta = 10.5$. The experimental correlations in Birouk & Gökalp (2006) suggests that, at high temperature and pressure i.e., when the evaporation is much faster than the turbulent time scale, the evaporation is only weakly dependent on the droplet size d_0/η. This is consistent with our results, where the difference in K for the two droplet sizes examined decreases when increasing the temperature; however, we do not observe the rate of evaporation to become independent of the size in the parameter range considered.

The variation of the evaporation rate with d_0/η significantly affects the liquid temperature at the interface $T_{\Gamma,l}$ (computed as the surface average over the gas-liquid interface, $T_{\Gamma,l} = (1/\Gamma)\int_\Gamma T d\Gamma$) and the mean liquid temperature $T_{V,l}$ (computed as the volume average over the liquid, $T_{V,l} = (1/V_l)\int_{V_l} T dV_l$). This is shown in figure 8 for the three temperatures under investigation. At the highest temperature, panel 8a, both $T_{\Gamma,l}$ and $T_{V,l}$ decrease with respect to the initial values due to the strong cooling caused by the evaporation. However, due to the heat transfer enhancement at higher $Re_{\mathcal{S}}$, $T_{\Gamma,l}$ remains greater than $T_{V,l}$ for droplets at larger d_0/η, whereas $T_{\Gamma,l}$ is lower than $T_{V,l}$ for the smaller d_0/η considered. Clearly, the two temperatures eventually converge to a similar value once the thermal gradients inside the liquid reduce. For the case with intermediate temperature, see panel 8b, the cooling due to evaporation is not sufficiently high to counteract the heat released from the gas and the two temperatures reach a regime value larger than the initial one. The final values of $T_{\Gamma,l}$ and $T_{V,l}$ are higher for the droplets with larger d_0/η (larger Reynolds number). We also note that the interface region is warmer than the droplet bulk (i.e., $T_{\Gamma,l} > T_{V,l}$) for both droplet sizes. At the lowest temperature,
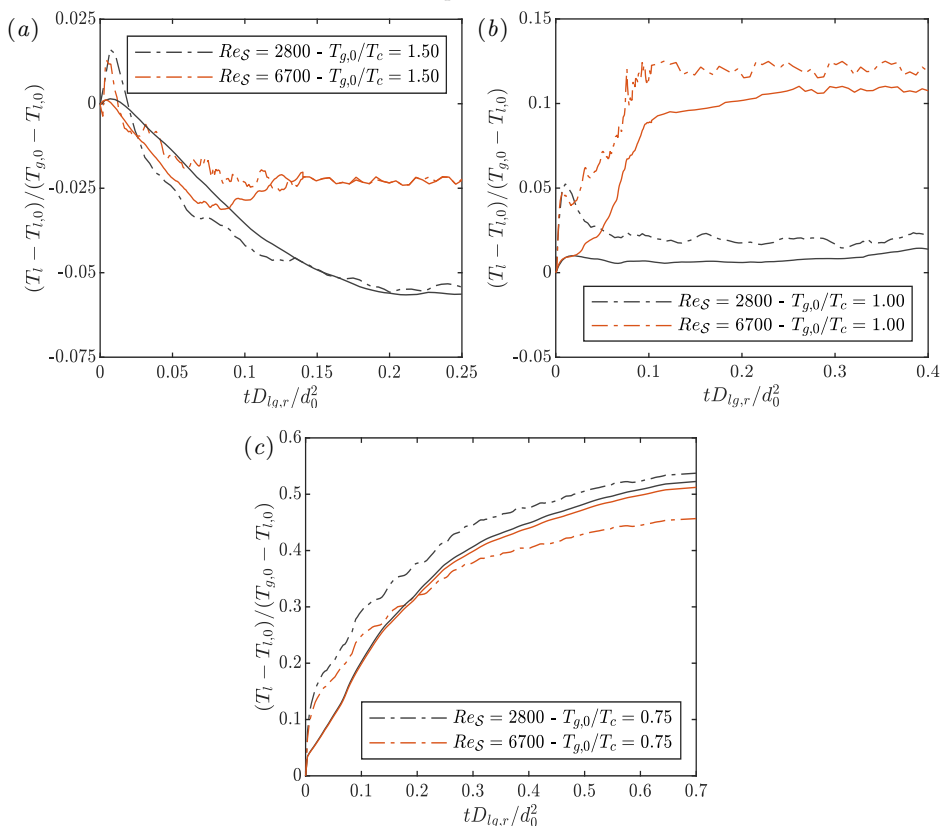
Figure 8: Dimensionless liquid temperature at the interface $(T_{l,\Gamma} - T_{l,0})/(T_{g,0} - T_{l,0})$ (dotted line) and average liquid temperature $(T_{l,V} - T_{l,0})/(T_{g,0} - T_{l,0})$ (continuous line) at a) $T_{g,0}/T_c = 1.5$, b) $T_{g,0}/T_c = 1.0$ and c) $T_{g,0}/T_c = 0.75$.

panel c of the figure 8, both $T_{\Gamma,l}$ and $T_{V,l}$ increase with time, when the evaporation is too slow to cool the droplets. Unlike the previous two cases, the values of $T_{\Gamma,l}$ and $T_{V,l}$ at $d_0/\eta = 21.5$ are always lower than the corresponding ones at $d_0/\eta = 10.5$, due to the higher evaporation rate at the highest $Re_{\mathcal{S}}$. For this case, the faster evaporation also changes the transient of $T_{\Gamma,l}$, which at the beginning is higher than $T_{V,l}$ while for $tD_{lg,r}/d_0 > 0.2$ becomes lower.

We conclude this section by analyzing the relative importance of the convective and conductive heat and mass vapor fluxes, $\mathcal{F}_{T,i=c,d}$ and $\mathcal{F}_{Y,i=c,d}$, in the gas region around the droplets and inside the liquid region. These are computed as integral over the control surfaces S_T and S_Y,

$$
\begin{aligned}
\mathcal{F}_{T,d} &= -\frac{1}{S_T} \int_{S_T} k\nabla T \cdot \mathbf{n}_\Gamma dS_T, \\
\mathcal{F}_{T,c} &= \frac{1}{S_T} \int_{S_T} \rho c_p \left(\mathbf{u}'T + \mathcal{S}z\mathbf{e}_x T\right) \cdot \mathbf{n}_\Gamma dS_T, \\
\mathcal{F}_{Y,d} &= -\frac{1}{S_Y} \int_{S_Y} \rho_g D_{lg} \nabla Y_l^v \cdot \mathbf{n}_\Gamma dS_Y, \\
\mathcal{F}_{Y,c} &= \frac{1}{S_Y} \int_{S_Y} \rho_g \left(\mathbf{u}'Y_l^v + \mathcal{S}z\mathbf{e}_x Y_l^v\right) \cdot \mathbf{n}_\Gamma dS_Y.
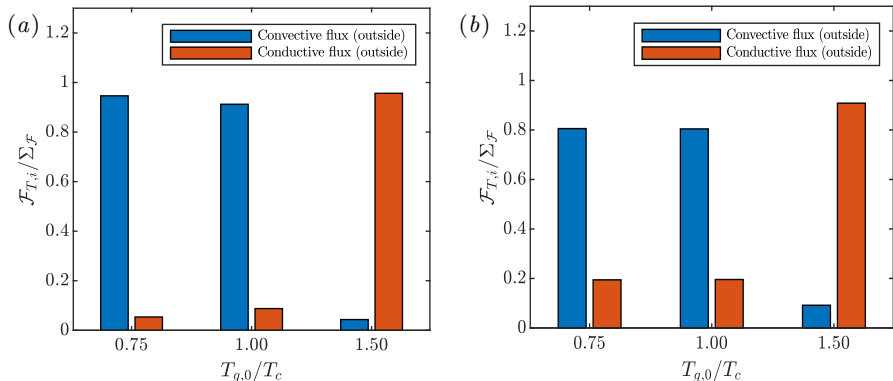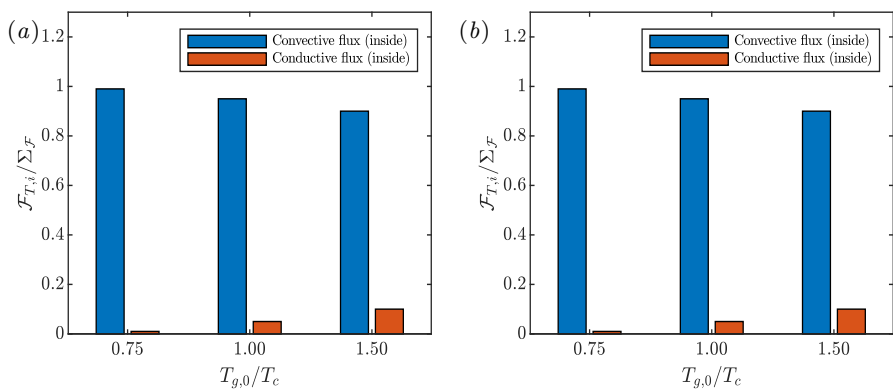\end{aligned}
\tag{4.7}
$$

Figure 9: Conductive and convective heat fluxes $\mathcal{F}_T$ (over the sum of the two, $\Sigma_{\mathcal{F}}$), $\mathcal{F}_{T,i=c,d}$, in the gas region for $T_{g,0}/T_c = 0.75 - 1.00 - 1.50$ and: a) $Re_{\mathcal{S}} = 6700$, b) $Re_{\mathcal{S}} = 2800$. At $Re_{\mathcal{S}} = 6700$, $\Sigma_{\mathcal{F},0.75} = 0.08\Sigma_{\mathcal{F},1.50}$ and $\Sigma_{\mathcal{F},1.00} = 0.14\Sigma_{\mathcal{F},1.50}$. At $Re_{\mathcal{S}} = 2800$, $\Sigma_{\mathcal{F},0.75} = 0.04\Sigma_{\mathcal{F},1.50}$ and $\Sigma_{\mathcal{F},1.00} = 0.13\Sigma_{\mathcal{F},1.50}$ (In $\Sigma_{\mathcal{F},x}$, x is the temperature ratio).

Figure 10: Conductive and convective heat fluxes $\mathcal{F}_T$ (over the sum of the two, $\Sigma_{\mathcal{F}}$), $\mathcal{F}_{T,i=c,d}$, in the liquid region for $T_{g,0}/T_c = 0.75 - 1.00 - 1.50$ and: a) $Re_{\mathcal{S}} = 6700$, b) $Re_{\mathcal{S}} = 2800$. At $Re_{\mathcal{S}} = 6700$, $\Sigma_{\mathcal{F},0.75} = 0.12\Sigma_{\mathcal{F},1.50}$ and $\Sigma_{\mathcal{F},1.00} = 0.24\Sigma_{\mathcal{F},1.50}$. At $Re_{\mathcal{S}} = 2800$, $\Sigma_{\mathcal{F},0.75} = 0.11\Sigma_{\mathcal{F},1.50}$ and $\Sigma_{\mathcal{F},1.00} = 0.48\Sigma_{\mathcal{F},1.50}$ (In $\Sigma_{\mathcal{F},x}$, x is the temperature ratio).

In the gas phase, S_T and S_Y are surfaces conforming to the droplet shape (quasi-spherical at this low value of $We_{\mathcal{S}}$) at a distance approximately equal to the thermal and vapor mass fraction boundary layer thicknesses δ_T and δ_Y. These are determined as the distance from the interface where $(T(\delta_T) - T_\Gamma)/(T_{g,0} - T_\Gamma) = 0.99$ and $(Y_l^v(\delta_Y) - Y_{l,\Gamma}^v)/(Y_{l,0}^v - Y_{l,\Gamma}^v) = 0.99$ as in Ni *et al.* (2021), moving normal to the interface thanks to a level-set function, reconstructed from the VoF field. We evaluate $\mathcal{F}$ as in equations (4.7) after the evaporation reaches a steady condition (i.e., d^2 regime) and average in time over a time interval $\Delta t = [0.20, 0.50, 0.60](tD_{lg,r})/d_0^2$ for the high, intermediate and low temperature ratios. To capture the dominant transport mechanism in the liquid phase, S_T is defined at a distance from the interface equal to half the instantaneous droplet radius.

The relative importance of the conductive and convective heat fluxes in the gas region are shown in figure 9: increasing the ratio $T_{g,0}/T_c$, the main transport mechanism changes from convection to conduction, as already anticipated in section 4.1 when discussing the
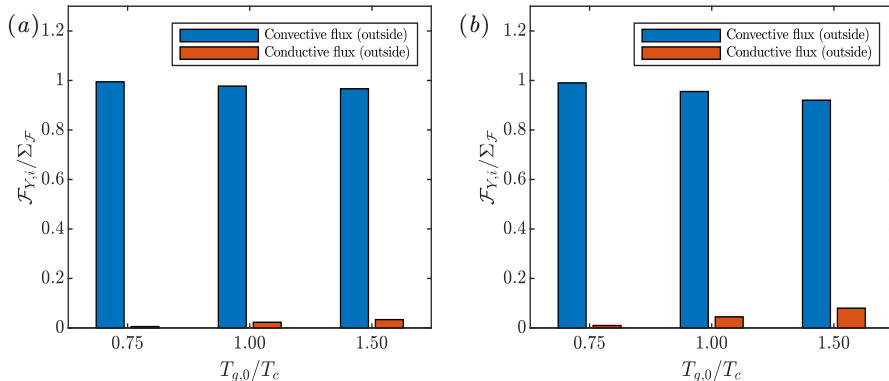
Figure 11: Conductive and convective vapour mass fluxes $\mathcal{F}_Y$ (over the sum of the two, $\Sigma_\mathcal{F}$), $\mathcal{F}_{Y,i=c,d}$, in the gas region for $T_{g,0}/T_c = 0.75 - 1.00 - 1.50$ and: a) $Re_\mathcal{S} = 6700$, b) $Re_\mathcal{S} = 2800$. At $Re_\mathcal{S} = 6700$, $\Sigma_{\mathcal{F},0.75} = 0.58\Sigma_{\mathcal{F},1.50}$ and $\Sigma_{\mathcal{F},1.00} = 0.89\Sigma_{\mathcal{F},T_{g,0}/T_c=1.50}$. At $Re_\mathcal{S} = 2800$, $\Sigma_{\mathcal{F},0.75} = 0.56\Sigma_{\mathcal{F},T_{g,0}/T_c=1.50}$ and $\Sigma_{\mathcal{F},1.00} = 0.87\Sigma_{\mathcal{F},1.50}$ (In $\Sigma_{\mathcal{F},x}$, x is the temperature ratio).

Sherwood number Sh. The same applies to lower $Re_\mathcal{S}$, where we observe a slightly higher conductive contribution for $T_{g,0}/T_c = 1.5$. In the liquid region, fig 10, the heat transport is mainly driven by convection in all cases. In agreement with previous experimental results (Wong & Lin 1992; Pinheiro *et al.* 2019), the dominant transport mechanism is weakly affected by a change of the droplet Reynolds number, here varied by changing $Re_\mathcal{S}$, since the motion of the liquid inside the droplet is not significantly affected by the intensity of the gas turbulence. Finally, the vapor fluxes reported in figure 11 show that Y_l^v is predominantly transported by convection for the two Reynolds numbers investigated, mass diffusion being relevant only at the highest temperatures.

4.3. *Effects of the shear-based Weber number*

At last, we consider the effect of the shear-based Weber number on the evaporation rate. For this analysis, three Weber numbers $We_\mathcal{S} = 0.02 - 0.06 - 0.10$ and two temperature ratios $T_{g,0}/T_c = 0.75 - 1.5$ are considered and, as for the previous section, the complete thermodynamic model (i.e., VP_a) is employed to evaluate the gas thermophysical properties. Figure 12a-b) reports the time evolution of d^2 for the three values of $We_\mathcal{S}$ under investigation at high and low temperatures, respectively. Increasing $We_\mathcal{S}$ leads to a higher evaporation rate, due to the increase of the surface area available for mass transfer as a consequence of deformation. Note, also, that the increase in the evaporation rate with $We_\mathcal{S}$ is more pronounced at lower temperature (see 12c), which can be explained by the fact that the evaporation is faster at higher temperatures, the droplets are therefore smaller, which leads to a limited deformation with respect to the cases at same $We_\mathcal{S}$ and $T_{g,0}/T_c = 0.75$. In other words, the effective Weber number based on the droplet diameter becomes quickly smaller at higher temperatures, so differences in nominal surface tension are compensated by the reduced droplet size. To quantify deformation while accounting for the decrease of the liquid volume, we measure the deviation from the initial spherical shape as the ratio between the instantaneous interfacial area A (computed numerically as $A = |\nabla\Phi|\Delta x^3$) and the area of a spherical droplet with same volume V, i.e., $A_{eq} = \pi^{1/3}(6V)^{2/3}$. This calculation is performed for each droplet q separately and each contribution $A_q/A_{eq,q}$ averaged according to the
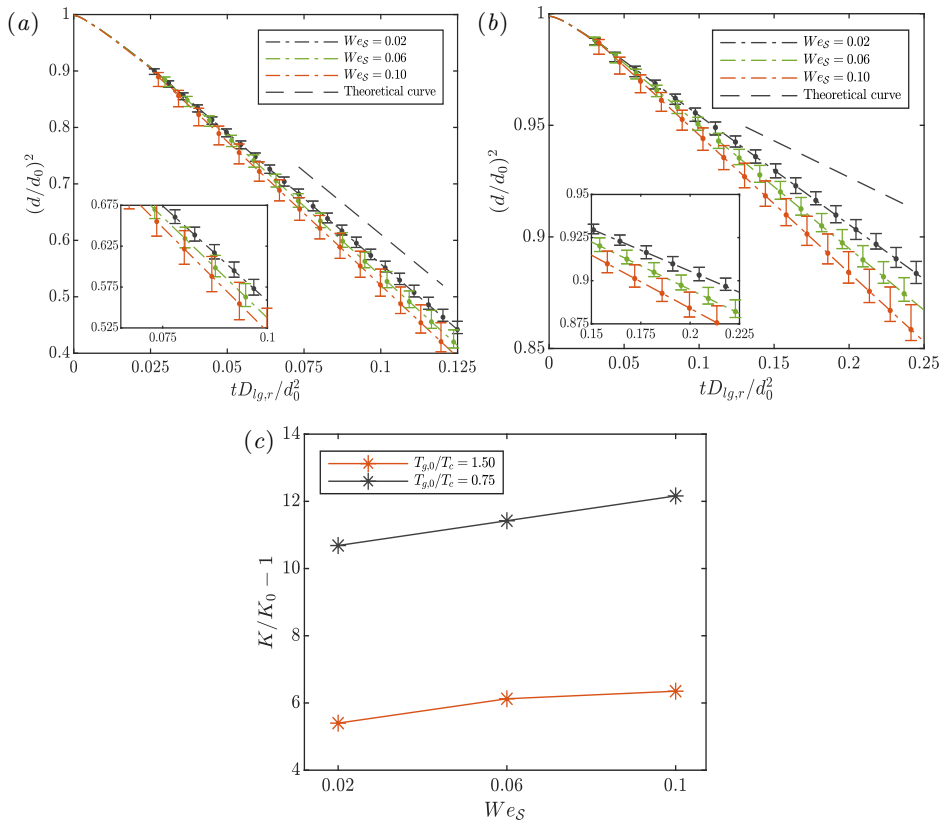
Figure 12: Time history of $(d/d_0)^2$ when varying the Weber number, $We_{\mathcal{S}} = 0.02 - 0.06 - 0.10$ and for temperature ratios a): $T_{g,0}/T_c = 1.50$ and b): $T_{g,0}/T_c = 0.75$. The black dashed curves represent the theoretical prediction of the actual evaporation rate obtained with the procedure explained in section 4.1. The length of the error bars (included for $tD_{lg,r}/d_0^2 > 0.025$ and $tD_{lg,r}/d_0^2 > 0.04$, respectively) indicates the droplet with the fastest/slowest evaporation rate among the five droplets in the simulations. c) Evaporation enhancement (i.e., K/K_0) as function of $We_{\mathcal{S}}$ for $Re_{\mathcal{S}} = 6700$ and $T_{g,0}/T_c = 0.75 - 1.50$.

instantaneous number of droplets, N_{dp}:

$$\frac{A}{A_{eq}} = \frac{1}{N_{dp}} \sum_{q=1}^{N_{dp}} \frac{A_q}{A_{eq,q}}. \qquad (4.8)$$

The time evolution of A/A_{eq} is reported in figure 13: as expected, the ratio A/A_{eq} increases with $We_{\mathcal{S}}$. For $T_{g,0}/T_c = 1.5$, the data in the figure also display two peaks: at $tD_{lg,r}/d_0^2 \approx 0.075 - 0.10$ for $We_{\mathcal{S}} = 0.10$ and $tD_{lg,r}/d_0^2 \approx 0.085 - 0.10$ for $We_{\mathcal{S}} = 0.06$. These are associated to the droplet breakup as we have $N_{dp} = 7$ droplets for $We_{\mathcal{S}} = 0.06$ and $N_{dp} = 9$ for $We_{\mathcal{S}} = 0.10$ at the end of the simulations. For $We_{\mathcal{S}} = 0.02$, no break-up events have been observed within the simulation time. For $T_{g,0}/T_c = 0.75$, given the lower evaporation rate and consequently the higher effective Weber number, breakups event have been observed for all the cases in the interval $0.05 < tD_{lg,r}/d_0^2 < 0.125$, finally yielding $N_{dp} = 7 - 9 - 12$ for $We_{\mathcal{S}} = 0.02 - 0.06 - 0.10$.
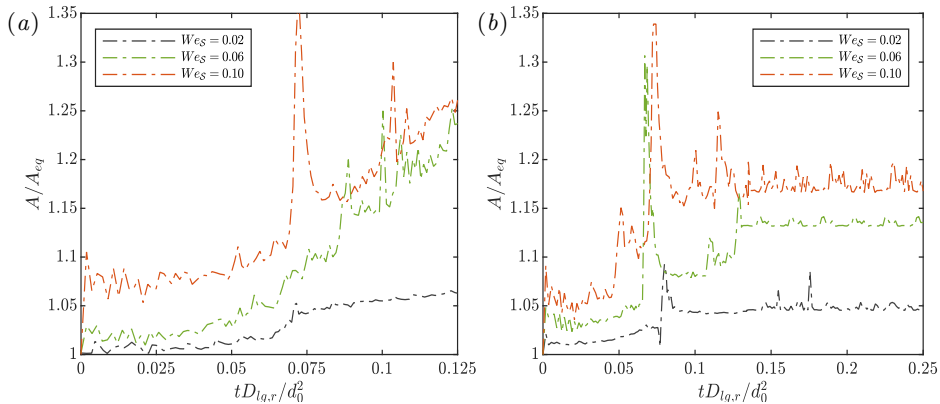
Figure 13: Ratio between the instantaneous interfacial area A and the area of a spherical droplet with same volume V, i.e., $A_{eq} = \pi^{1/3}(6V)^{2/3}$, for $We_{\mathcal{S}} = 0.02 - 0.06 - 0.10$ and a): $T_{g,0}/T_c = 1.50$ and b): $T_{g,0}/T_c = 0.75$.

Interestingly, for the case $T_{g,0}/T_c = 0.75$, A/A_{eq} approaches a statistically stationary value for $tD_{lg}/d_0^2 > 0.125$, whereas a regime value is not reached in the investigated time window for $T_{g,0}/T_c = 1.50$. This behavior is interpreted by comparing the time scale of deformation as dictated by surface tension and applied shear, τ_σ, with the time scale of evaporation extracted from the simulations, τ_v:

$$\Pi_{\sigma v} = \frac{\tau_\sigma}{\tau_v}, \qquad (4.9)$$

where $\tau_\sigma = \rho_{g,r}(\mathcal{S}d_0)d_0^2/\sigma$ and $\tau_v = d_0^2/K$, with K the evaporation at statically steady state, see figure 14. At the high temperature ratio, evaporation is faster than deformation (i.e., $\tau_\sigma > \tau_v$) and the surface tension does not have time to adjust the droplet shape after the mass losses due to the differential evaporation across the interface. An increasing deviation from the spherical shape is therefore observed in time. Conversely, at low temperature, the deformation time is comparable or lower than the evaporation time (i.e., $\tau_\sigma < \tau_v$) and the droplet shape can compensate for the local deformations induced by the evaporation mass flux (note that the droplet tend to a constant deformation, increasing with $We_{\mathcal{S}}$ and not to the spherical shape, i.e. $A/A_{eq} > 1$, as we have an imposed shear). From the data in figure 14, we also notice that for a fixed $T_{g,0}/T_c$, increasing $We_{\mathcal{S}}$ accelerates the evaporation time-scale (i.e., higher $\Pi_{\sigma v}$), consistently with what observed in figure 12.

Given the variation of the evaporation rate with the $We_{\mathcal{S}}$, it is worth investigating whether the evaporation flux at the droplet surface is correlated to the local curvature. This has been already assessed in laminar flows analytically for evaporating droplets of spheroidal shapes (Tonini & Cossali 2013), and experimentally for sessile droplets (Sáenz et al. 2017). In turbulent flows, this analysis is missing and is performed here by computing the joint probability density function (joint p.d.f.) of the normalized interfacial mean curvature $\kappa_\Gamma/\kappa_{\Gamma,eq}$ and the dimensionless interfacial mass-flux $\dot{m}_\Gamma/\dot{m}_{\Gamma,0}$, where $\kappa_{\Gamma,eq}$ is the curvature of a spherical droplet with same volume V (i.e., $\kappa_{\Gamma,eq} = 4/d_{eq}$ with $d_{eq} = (6V/\pi)^{1/3}$) and $\dot{m}_{\Gamma,0}$ is the interfacial mass-flux for a purely diffusion-dominated evaporation process, i.e.,

$$\dot{m}_{\Gamma,0} = 8\pi\rho_{g,r}D_{lg,r}\log(1 + B_M)/d_0. \qquad (4.10)$$

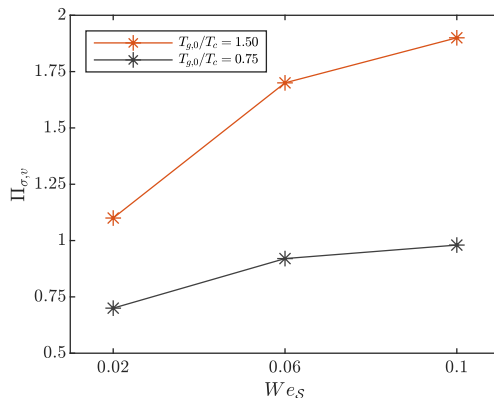Note that $\dot{m}_\Gamma$ is evaluated using the expression (2.5) in all the nodal points cut by the

Figure 14: Ratio between the deformation time scale and the evaporation time scale (in turbulent condition) as a function of $We_{\mathcal{S}}$ for $T_{g,0}/T_c = 0.75$ and 1.50.
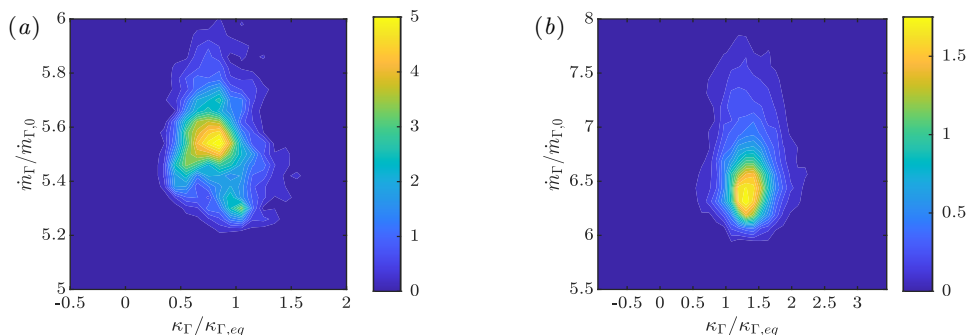

Figure 15: Joint p.d.f. of the dimensionless mass flux $\dot{m}_{\Gamma}/\dot{m}_{\Gamma,0}$ and the normalized interfacial curvature $\kappa_{\Gamma}/\kappa_{\Gamma,eq}$ for $Re_{\mathcal{S}} = 6700$, $T_{g,0}/T_c = 1.5$ and a) $We_{\mathcal{S}} = 0.02$, b) $We_{\mathcal{S}} = 0.10$.

interface, whereas κ_{Γ} is computed directly from its definition, i.e., $\kappa_{\Gamma} = \nabla \cdot \mathbf{n}_{\Gamma}$. The reconstructed level-set function is employed for a more accurate estimation of κ_{Γ}.

From the results at high temperature (i.e., $T_{g,0}/T_c = 1.5$) reported in figure 15, we do not note a clear relation between $\dot{m}_{\Gamma}$ and κ_{Γ}, yet there is a relatively broad distribution of mass fluxes over the droplet surface, which can be attributed to the local variations of vapor concentrations in the gas phase induced by the turbulence and by the flow anisotropy. Indeed, the regions whose local outward normal vector is parallel to the mean flow direction (i.e., droplet front) experience higher surface vapor gradients, whereas larger concentration are found in those where the normal vector is opposite to the flow (i.e, droplet rear). Note also that the increase of $We_{\mathcal{S}}$ corresponds to a shift of the most probable values of $\dot{m}_{\Gamma}$ and κ_{Γ} towards higher values.

When the gas temperature is reduced (i.e., $T_{g,0}/T_c = 0.75$), the correlation between $\dot{m}_{\Gamma}$ and κ_{Γ} is still weak for $We_{\mathcal{S}} = 0.02$, while for the case at $We_{\mathcal{S}} = 0.10$ a higher interfacial curvature is associated with a higher interfacial mass-flux. Also at lower temperatures, the most probable values are located at higher κ_{Γ} when increasing the Weber number. Comparing with the results at higher temperatures, figure 15, we note that $\dot{m}_{\Gamma}/\dot{m}_{\Gamma,0}$ is larger: turbulence enhances evaporation more efficiently at low temperature, when the evaporative time scale is longer and the ratio with the turbulent time scales decreases,
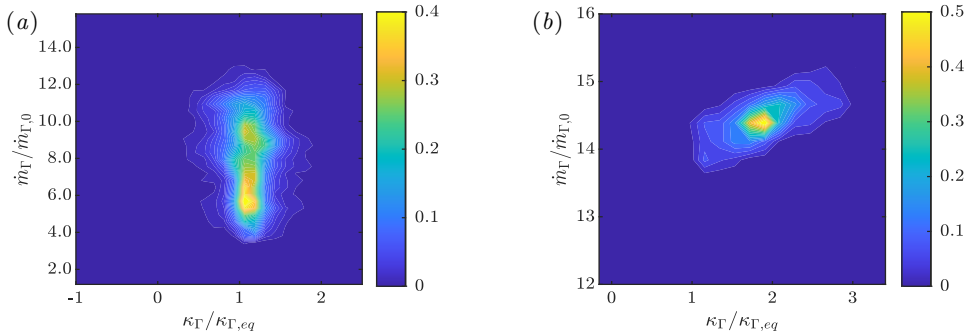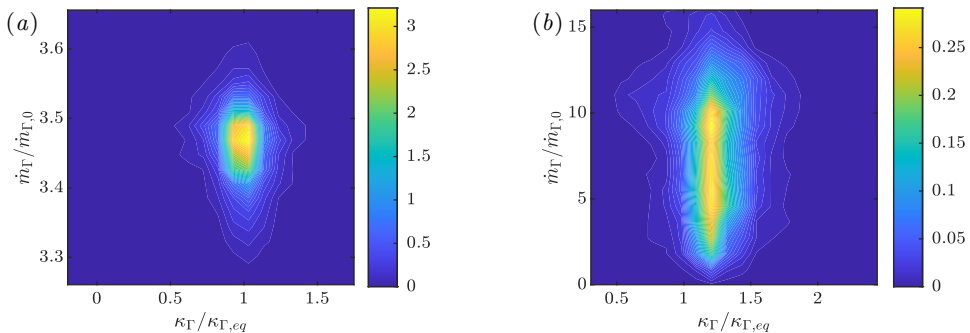
Figure 16: Joint p.d.f. of the dimensionless mass flux $\dot{m}_\Gamma/\dot{m}_{\Gamma,0}$ and the normalized interfacial curvature $\kappa_\Gamma/\kappa_{\Gamma,eq}$ for $Re_\mathcal{S} = 6700$, $T_{g,0}/T_c = 0.75$ and a) $We_\mathcal{S} = 0.02$, b) $We_\mathcal{S} = 0.10$.

Figure 17: Joint p.d.f. of the dimensionless mass flux $\dot{m}_\Gamma/\dot{m}_{\Gamma,0}$ and the normalized interfacial curvature $\kappa_\Gamma/\kappa_{\Gamma,eq}$ for $Re_\mathcal{S} = 2800$ for $We_\mathcal{S} = 0.02$ and a) $T_{g,0}/T_c = 1.50$ and b) $T_{g,0}/T_c = 0.75$.

i.e. Da_v decreases.

Finally, we display in figure 17 the joint p.d.f. from the simulations at lower Reynolds number, $Re_\mathcal{S} = 2800$, for $T_{g,0}/T_c = 0.75 - 1.5$ and $We_\mathcal{S} = 0.02$. In this case, the reduction of $T_{g,0}/T_c$ leads to more pronounced deformation, i.e. larger values of $\kappa_\Gamma/\kappa_{\Gamma,eq}$ (due to the slower evaporation and higher effective $We_\mathcal{S}$) and to higher values of $\dot{m}_\Gamma/\dot{m}_{\Gamma,0}$ (more pronounced effects of turbulence at lower absolute evaporation rates) and a broader distribution, again attributed to fluctuations induced by the turbulence. Comparing with the results at the same $We_\mathcal{S}$ and $T_{g,0}/T_c$ but $Re_\mathcal{S} = 6700$ in panels (a) of figures 15 and 16, we see that, for both temperature ratios, the reduction in $Re_\mathcal{S}$ restricts the range of attained values for the curvature and the ratio $\dot{m}_\Gamma/\dot{m}_{\Gamma,0}$, confirming that the increase of deformation and evaporation rate is more pronounced for bigger droplets.

5. Conclusions

Fully resolved simulations of finite size evaporating droplets are performed in homogeneous shear turbulence using a weakly-compressible solver for evaporating flows. The new methodology, here described, combines two features. First, an improved version of the Adams-Bashforth method in order to address the limitations of the classical formulation, already highlighted in Kasbaoui *et al.* (2017). The improvement allows to match the single phase analytical solution in the Rapid Distorsion Limit and ensures

a stable integration over long times. Second, a mathematical model with the details of the numerical implementation for a two-phase evaporating system composed of an incompressible liquid and a compressible gas phase. In order to remove the acoustic time-step restriction, compressible effects are here handled in the low-Mach number limit. This new methodology is applied to investigate the behavior of finite-size evaporating droplets in HST when changing the gas temperature over the critical temperature $T_{g,0}/T_c = 0.75, 1.00$ and 1.50, the initial droplet diameter in terms of Kolmogorov scale, $d_0/\eta = 10.5$ and 21.5 and the surface tension, quantified by the shear-based Weber number $We_{\mathcal{S}} = 0.02, 0.06$ and 0.10.

First, using the data at $d_0/\eta = 21.5$ and $We_{\mathcal{S}} = 0.02$, we study the differences when employing different thermodynamic models for the gas thermophysical properties. Three approaches are investigated: a constant property model where the gas properties are kept constant and initialized with the "1/3 rule" (CP) and two variable-properties approaches where either the gas density, VP_ρ or all the gas properties are allowed to vary, VP_a. We find that the predictions by the CP and VP_a models agree well, whereas the VP_ρ model overpredicts the evaporation rate, especially at high temperature. This overestimation occurs since the local increase of the gas density (due to evaporative cooling) is captured by the VP_ρ model, but the decrease of the diffusion coefficient with temperature, which slows down the evaporation, is not accounted. Moreover, by extracting the Sherwood number for the three models at $T_{g,0}/T_c = 0.75, 1.50$ and comparing it with the Frössling/Ranz-Marshall correlation (Ranz *et al.* 1952), we show that the correlation provides an excellent estimation of Sh at high temperature (conduction dominated regime), whereas it substantially underestimates Sh at lower temperature (convective dominated regime), in agreement with recent experimental observations (Méès *et al.* 2020).

Next, reducing the ratio d_0/η from 21.5 to 10.5 (obtained by reducing $Re_{\mathcal{S}}$ from 6700 to 2800), we show that the ratio between the actual evaporation rate, and the one computed in stagnant condition, is always much higher than 1, while decreasing with $T_{g,0}/T_c$. Interestingly, this ratio does not approach unity at the highest temperature level, suggesting an evaporation enhancement due to turbulence also in these conditions. The variation of the droplet size, d_0/η, also affects the liquid temperature at the interface and the mean liquid temperature. For $T_{g,0}/T_c = 1.0, 1.5$, the regime values of both quantities are larger for droplets of $d_0/\eta = 21.5$, whereas the opposite is true at $T_{g,0}/T_c = 0.75$ when the regime values of the liquid temperature are lower for the largest droplets. This is explained as the result of two competing effects: cooling by evaporation and heating from the hot gas.

Finally, by varying $We_{\mathcal{S}}$ in the range 0.02 and 0.10, we observe an increase in the evaporation rate for higher $We_{\mathcal{S}}$ given the larger surface area available for mass transfer. At fixed $We_{\mathcal{S}}$, this increase is more pronounced at $T_{g,0}/T_c = 0.75$ due to slower evaporation rate and to a higher deformation (larger effective Weber number based on the instantaneous droplet diameter). By computing the joint p.d.f. of the interfacial mass-flux and curvature, a weak correlation between the two is observed at high temperature regardless of the Weber number, whereas a positive correlation is recovered at $T_{g,0}/T_c = 0.75$ and $We_{\mathcal{S}} = 0.10$, consistently with the theoretical prediction in laminar environments (Tonini & Cossali 2013) and the experimental observations for sessile droplets (Sáenz *et al.* 2017).

Note that in all the cases, the initial liquid volume fraction has been kept small (i.e., $\alpha_0 \approx 0.14\%$), the droplets do not interact with each other and, as expected, no significant deviations from the the d^2 law have been observed. To investigate such deviations and more in general the collective dynamics of a dense suspension of evaporating droplets we

are currently exploring the same configurations presented in this work at higher volume fractions.

Acknowledgements

Appendix A. Equations of state

In this appendix, we report the equations of state employed for the the gas density, the gas thermal diffusivity, the gas viscosity, thermal conductivity, heat capacity at constant pressure and the Span-Wagner equation of state.

A.1. *Gas density*

The gas density variations as a function of p_{th}, T_g and Y_l^v follow the ideal gas model:

$$\rho_g = \Pi_{p,2} \frac{p_{th}\overline{M}_{m,av}}{T_g}, \tag{A 1}$$

where $\overline{M}_{m,av}$ is the mixture molar mass computed using an harmonic average between the gas and the liquid molar mass and $\Pi_{p,2} = (p_{th,r}M_g)/(R_u T_{g,r})$ where $p_{th,r}$ and $T_{g,r}$ are the reference thermodynamic pressure and gas temperature, taken equal to the corresponding initial value and R_u is the universal gas constant.

A.2. *Liquid-gas diffusion coefficient*

The liquid gas diffusion coefficient is computed using the following relation (Reid *et al.* 1987):

$$D_{lg} = \frac{T_g^{3/2}}{p_{th}}, \tag{A 2}$$

where T_g is the gas temperature.

A.3. *Gas viscosity*

The gas viscosity varies with the temperature according to the simplified Sutherland's law (Reid *et al.* 1987):

$$\mu_g = T_g^{2/3}. \tag{A 3}$$

A.4. *Specific heat capacity at constant pressure*

The specific heat capacity at constant pressure is evaluated as function of the temperature using the virial polynomials (Reid *et al.* 1987):

$$c_p = A_1 + A_2 T_g + A_3 T_g^2 + A_4 T_g^3 + A_5 T_g^4, \tag{A 4}$$

where the coefficients $A_1 = 1.012$, $A_2 = 0.0553$, $A_3 = 0.006$, $A_4 = 2 \cdot 10^{-3}$ and $A_5 = 5 \cdot 10^{-4}$ are adequate to estimate the heat capacity at constant pressure for dry air over a wide range of temperature.

A.5. *Gas thermal conductivity*

As for the gas viscosity, the gas thermal conductivity is function of the temperature only and computed as (Reid *et al.* 1987):

$$k_g = \frac{\mu_g c_{pg}}{Pr},\qquad(A\,5)$$

where Pr is the Prandtl number.

A.6. *SpanWagner equation of state*

In order to compute the value of Y_l^v at the interface, see section 3.1.2, we assume that the gas mixture is ideal and composed of ideal components. Hence, $Y_{l,\Gamma}^v$ can be computed using the Rault's law:

$$Y_{l,\Gamma}^v = \frac{\dfrac{p_{s,\Gamma}}{p_{th}}}{\dfrac{p_{s,\Gamma}}{p_{th}} + \left(1 - \dfrac{p_{s,\Gamma}}{p_{th}}\right)\dfrac{1}{\lambda_M}},\qquad(A\,6)$$

where $\lambda_M = M_l/M_g$ is the molar mass ratio, while p_{th} and $p_{s,\Gamma}$ are the thermodynamic pressure and the partial pressure of the vaporized species at the interface. Since the interface is assumed at saturation, $p_{s,\Gamma}$ is computed as function of the liquid temperature at the interface. For most of the substances, the Span-Wagner equation of state represents a valid approximation over a wide range of thermodynamic pressure and temperature (Span & Wagner 1996):

$$\frac{p_{s,\Gamma}}{p_{th}} = \frac{\Pi_{p,3}}{p_{th}} \exp\left[\frac{B_1\eta_{sw} + B_2\eta_{sw}^{1.5} + B_3\eta_{sw}^{2.5} + B_4\eta_{sw}^{5}}{1 - \eta_{sw}}\right].\qquad(A\,7)$$

where $\eta_{sw} = 1 - T_\Gamma(T_{g,0}/T_c)$ and $\Pi_{p,3} = p_c/p_{th,r}$ with $T_{g,0}$, T_c and p_c the initial gas temperature, the critical temperature and critical pressure, respectively. The coefficients $B_{i=1,4} = \{-7.32714, 1.82365, -2.272744, -2.711929\}$ are experimentally determined and correspond in the current study to those of pentane, see Span & Wagner (1996). Note that the use of the Span-Wagner model is also convenient since it does not involve the saturation temperature (like the ClausiusClapeyron relation), which in a weakly-compressible phase-changing system is not a constant anymore, but should be computed as a function of the time-varying thermodynamic pressure.

As a final remark, to justify the assumption of incompressible liquid with constant properties, we evaluate a posteriori the variations of ρ_l, c_{pl}, k_l and μ_l given the maximum variation of liquid temperature discussed in section 4.2. Using the data reported in Reid *et al.* (1987) and taking as reference the cases at $T_{g,0}/T_c = 1.5$ (when the liquid temperature variation is more pronounced), these amount to: $\Delta\rho_l/\rho_{l,0} = 6\,\%$, $\Delta\mu_l/\mu_{l,0} = 8\,\%$, $\Delta c_{pl}/c_{pl,0} = 4\,\%$, $\Delta k_l/k_{l,0} = 5\,\%$.

Appendix B. Derivation of the velocity divergence

The system composed of equations (2.2), (2.3),(2.5) and (2.4) reported in section 2 is not closed and an additional equation should be included. To derive it, we adapt the approach proposed in Majda & Sethian (1985) in the context of reacting flows and

recently employed for phase change in Dodd *et al.* (2021). Nevertheless, since a detailed derivation is missing in literature, it is provided here for completeness. The idea is to compute the missing relation from the divergence of the velocity field, $\mathbf{u}$, which can be computed as $H\mathbf{u}_l + (1 - H)\mathbf{u}_g$. Taking the divergence yields

$$\nabla \cdot \mathbf{u} = (\mathbf{u}_g - \mathbf{u}_l) \cdot \nabla H + (1 - H)\nabla \cdot \mathbf{u}_g + H\nabla \cdot \mathbf{u}_l. \tag{B 1}$$

The first term on the right-hand side represents the volume variation at the interface due to phase change, while the second and the third come from the density variations in the gas and in the liquid phase. We start with the phase-change contribution and consider a reference frame moving with the interface. Accordingly, we decompose the vector $\mathbf{u}_g - \mathbf{u}_l$ along the normal $\mathbf{n}_\Gamma$, tangential $\mathbf{t}_\Gamma$ and bi-normal directions $\mathbf{n}_\Gamma$:

$$\mathbf{u}_g - \mathbf{u}_l = (u_{g,n} - u_{l,n})\mathbf{n}_\Gamma + (u_{g,t} - u_{l,t})\mathbf{t}_\Gamma + (u_{g,b} - u_{l,b})\mathbf{b}_\Gamma. \tag{B 2}$$

If the interface has zero-thickness, the mass balance imposes that the velocity is continuous along the tangential and bi-normal direction (i.e., $u_{g,t} = u_{l,t}$ and $u_{g,b} = u_{l,b}$). Along the normal direction, conversely, the velocity has a discontinuity proportional to the mass-flux $\dot{m}_\Gamma$ between the two phases, i.e.,

$$\begin{aligned} \dot{m}_\Gamma &= \rho_{g,\Gamma}(u_{g,n} - u_{\Gamma,n}), \\ \dot{m}_\Gamma &= \rho_{l,\Gamma}(u_{l,n} - u_{\Gamma,n}), \end{aligned} \tag{B 3}$$

where $u_{\Gamma,n}$ represents the normal component of the interface velocity and $\rho_{i=l,g,\Gamma}$ the phase density at the interface location. Combining the previous two equations yields

$$u_{g,n} - u_{l,n} = \dot{m}_\Gamma \left(\frac{1}{\rho_{g,\Gamma}} - \frac{1}{\rho_{l,\Gamma}} \right). \tag{B 4}$$

Inserting equations (B 2) and (B 4) into in equation (B 1), we obtain

$$(\mathbf{u}_g - \mathbf{u}_l) \cdot \nabla H = \dot{m}_\Gamma \left(\frac{1}{\rho_{g,\Gamma}} - \frac{1}{\rho_{l,\Gamma}} \right) \delta_\Gamma, \tag{B 5}$$

where $\delta_\Gamma = \nabla H \cdot \mathbf{n}_\Gamma$.

The second term of equation (B 1) is computed from the continuity in the gas region. If chemical reactions are absent, this reads

$$\nabla \cdot \mathbf{u}_g = -\frac{1}{\rho_g} \frac{D\rho_g}{Dt}. \tag{B 6}$$

Using the equation of state for the gas density (A 1), the total derivative of ρ_g can be expanded as follows:

$$\frac{1}{\rho_g} \frac{D\rho_g}{Dt} = \frac{1}{p_{th}} \frac{Dp_{th}}{Dt} - \frac{1}{T} \frac{DT}{Dt} - \overline{M}_{m,av} \frac{D}{Dt} \left(\frac{1}{\overline{M}_{m,av}} \right). \tag{B 7}$$

Combining eq. (B 5) and (B 7) finally provides the velocity divergence in the gas region Dodd *et al.* (2021):

$$\nabla \cdot \mathbf{u}_g = -\frac{1}{p_{th}} \frac{dp_{th}}{dt} + \frac{1}{T} \frac{DT}{Dt} + \overline{M}_{m,av} \frac{D}{Dt} \left(\frac{1}{\overline{M}_{m,av}} \right). \tag{B 8}$$

Note that, given the low-Mach assumption, the total derivative of p_{th} in (B 8) has been replaced by the time derivative of p_{th}. A similar strategy can be employed to compute $\nabla \cdot \mathbf{u}_l$; however, we consider here constant and uniform liquid density and therefore, $\nabla \cdot \mathbf{u}_l = 0$ in eq. (B 1) and $\rho_{l,\Gamma} = \rho_l$.

Differently from what it is commonly done in literature (Motheau & Abraham 2016), we found preferable to replace the total derivative of the molar mass and of the temperature with the corresponding spatial derivatives. By doing so, this solution completely removes the time discretization errors when computing the terms in (B 8). For the contribution due to composition, we employ equation (2.3) and we treat the mixture of inert gas and vapor as ideal, so that the mixture molar mass is given by the harmonic average of the molar mass of each component (Reid *et al.* 1987). Accordingly, using the relation $Y_g = Y_N = 1 - \sum_{j=1}^{N-1} Y_{l,j}^v$ the third term on the right hand side of equation (B 8) becomes:

$$\overline{M}_{m,av} \frac{D}{Dt}\left(\frac{1}{\overline{M}_{m,av}}\right) = \overline{M}_{m,av} \sum_{j=1}^{N-1}\left(\frac{1}{\lambda_{M,j}} - 1\right)\frac{DY_{l,j}^v}{Dt}. \quad (B\,9)$$

where $\lambda_{M,j} = M_{l,j}/M_g$. For the temperature T, we start from the generic enthalpy equation for the gas phase:

$$\rho \frac{Dh}{Dt} = \frac{1}{RePr}\nabla\cdot(k\nabla T) + \Pi_{p,1}\frac{dp_{th}}{dt} + \frac{1}{ReSc}\sum_{j=1}^{N} h_j^v \nabla\cdot(\rho_g D_{lg}\nabla Y_j). \quad (B\,10)$$

In a weakly-compressible system, being the enthalpy of the gas phase function of temperature, thermodynamic pressure and vapour composition, the left-hand side of (B 10) can be expanded as:

$$\rho\frac{Dh}{Dt} = \rho\left(\frac{\partial h}{\partial T}\right)_{Y_{l,j}^v, p_{th}} \frac{DT}{Dt} + \rho\left(\frac{\partial h}{\partial p_{th}}\right)_{Y_{l,j}^v, T}\frac{dp_{th}}{dt} + \rho\sum_{j=1}^{N-1}\left(\frac{\partial h}{\partial Y_{l,j}^v}\right)_{T, Y_{i\neq j}}\frac{DY_{l,j}^v}{Dt},$$

$$= \rho c_p\frac{DT}{Dt} + \rho(1 - \beta T)\frac{dp_{th}}{dt} + \rho\sum_{j=1}^{N-1}\left(\frac{\partial h}{\partial Y_{l,j}^v}\right)_{T, p_{th}, Y_{l,i\neq j}^v}\frac{DY_{l,j}^v}{Dt}. \quad (B\,11)$$

Note that for an ideal gas, the isothermal compressibility coefficient $\beta = 1/T$ and, thus, $(1 - \beta T) = 0$, which can be omitted. Considering the term varying with the composition $Y_{l,j}^v$, this can be recast as (see Lupo *et al.* 2019, for details):

$$\sum_{j=1}^{N-1}\left(\frac{\partial h}{\partial Y_{l,j}^v}\right)_{T, p_{th}, Y_{l,i\neq j}^v}\frac{DY_{l,j}^v}{Dt} = \sum_{j=1}^{N-1}(h_{v,j} - h_g)\frac{DY_{l,j}^v}{Dt}. \quad (B\,12)$$

Inserting equations (B 12) and (B 11) into equation (B 10) and using (2.3), we get

$$\rho c_p\frac{DT}{Dt} = \frac{1}{RePr}\nabla\cdot(k\nabla T) + \left(\Pi_{p,1}\frac{dp_{th}}{dt} + \frac{\rho_g}{ReSc}\sum_{j=1}^{N} D_{lg,j}\nabla h_j\cdot\nabla Y_j\right)(1 - H). \quad (B\,13)$$

Note that equation (B 13) is the same as (2.4) expect for the source term due to phase change which acts at the interface location. Finally, by combining (B 13), (B 9) (B 8) in

the expression (B 1), the velocity divergence **u** can be expressed as:

$$\nabla \cdot \mathbf{u} = \underbrace{\dot{m}_\Gamma \left(\frac{1}{\rho_{g,\Gamma}} - \frac{1}{\lambda_\rho} \right) \delta_\Gamma}_{f_\Gamma(\mathbf{x}_\Gamma, t)},$$

$$+ \underbrace{\frac{1}{p_{th}} \frac{1}{ReSc} \frac{\overline{M}_{m,av}}{\rho_g} \sum_{j=1}^{N-1} \left(\frac{1}{\lambda_{M,j}} - 1 \right) \nabla \cdot (\rho_g D_{lg,j} \nabla Y_{l,j}^v)(1-H)}_{f_Y(\mathbf{x}, t)},$$

$$+ \underbrace{\frac{1}{p_{th}} \frac{1}{Re} \frac{\Pi_{p,1}}{c_p \overline{M}_{m,av}} \left[\frac{1}{Pr} \nabla \cdot (k\nabla T) + \frac{\rho_g}{Sc} \sum_{j=1}^{N} D_{lg,j} \nabla h_j \cdot \nabla Y_j \right] (1-H)}_{f_T(\mathbf{x}, t)}$$

$$- \left(1 - \frac{\Pi_{p,1}}{c_p \overline{M}_{m,av}} \right) \frac{1}{p_{th}} \frac{dp_{th}}{dt} (1-H), \tag{B 14}$$

where f_Γ, f_Y and f_T are functions representing the different contributions to the total velocity divergence, i.e., phase change, (f_Γ), change of the gas density due to composition (f_Y) and due to temperature (f_T).

The last step is to derive an expression for the thermodynamic pressure, p_{th}. For an open domain, p_{th} is constant, whereas for a closed or triperiodic domain it can be obtained by imposing the volume conservation on the global domain V. This can formally expressed as a constrain on the velocity divergence

$$\int_V \nabla \cdot \mathbf{u} \, dV = 0. \tag{B 15}$$

By employing (B 15), we can easily rearrange the rate of change of p_{th} as

$$\frac{1}{p_{th}} \frac{dp_{th}}{dt} \int_{V_g} \left(1 - \frac{\Pi_{p,1}}{c_p \overline{M}_{m,av}} \right) dV_g = \int_V \left[f_\Gamma(\mathbf{x}_\Gamma, t) + \frac{(f_T(\mathbf{x}, t) + f_Y(\mathbf{x}, t))}{p_{th}} (1-H) \right] dV. \tag{B 16}$$

Appendix C. Verification/Validation of the low Mach solver with phase change

In this appendix, we provide a verification and two validation cases of the weakly-compressible code employed to perform the numerical simulations in the present work.

C.1. *Droplet evaporation due to a prescribed, constant mass flux*

The set-up of this verification case consists of a two-dimensional circular droplet with initial diameter d_0, which evaporates due to a prescribed, constant mass-flux $\dot{m}_{\Gamma,A}$. In this case, the momentum equation is decoupled from the transport of energy and vapor mass fraction equations and it is straightforward to show that the droplet diameter evolves as:

$$\frac{d(t)}{d_0} = 1 - \left(\frac{2\dot{m}_{\Gamma,A}}{d_0 \rho_l} \right) t. \tag{C 1}$$

In our previous work (Scapin *et al.* 2020), we reproduce this test case using zero-pressure outflow boundary condition, whereas here we prescribe periodic boundary conditions. Accordingly, as evaporation starts, the thermodynamic pressure builds up and eventually
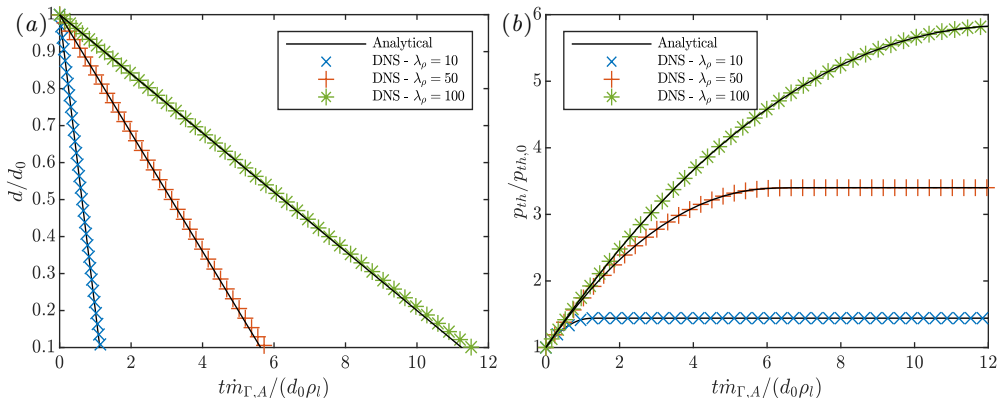
Figure 18: a): Temporal evolution of the instantaneous droplet diameter over the initial value, d/d_0, b): Temporal evolution of the thermodynamic pressure over the initial value, $p_{th}/p_{th,0}$.

reaches a stationary value when the droplet is completely evaporated. By setting f_Y and f_T to zero in equation (B 16) and after some manipulations a non-linear ordinary differential equation can be derived for p_{th}:

$$\frac{dp_{th}(t)}{dt} - \frac{42\dot{m}_{\Gamma,A}\pi d^2(t)}{30G_{tot} - 5\rho_l\pi d^3(t)} \left(1 - \frac{p_{th}(t)}{\rho_l(R_u/M_g)T_0}\right) p_{th}(t) = 0, \qquad (C\,2)$$

where $d(t)$ is computed using equation (C 1), G_{tot} is the mass inside the system, taken equal to its initial value (i.e., $G_{tot} = \rho_{g,0}V_{g,0} + \rho_l V_{l,0}$), T_0 and (R_u/M_g) are chosen so that the group $p_{th,0}/(\rho_{g,0}(R_u/M_g)T_0) = 1$. Equation (C 2) is here solved with the 4th order Runge-Kutta scheme. The test has been repeated for three density ratios $\lambda_\rho = 10-50-100$, with the remaining dimensionless physical parameters $Re = 25$, $We = 0.10$, $\lambda_\mu = 50$; gravity is absent. The governing equations are solved in a square domain $[-2d_0; 2d_0]^2$, discretized with 128×128 grid points. The droplet is held at the center of the domain. Results are reported in figure 18: an excellent agreement between the numerical and the analytical solutions is found for all the cases.

C.2. *Hexadecane static droplet evaporation in a hot gas*

As a validation case, we reproduce the numerical test proposed in Ni *et al.* (2021) consisting of a static hexadecane droplet of initial diameter $d_0 = 550~\mu m$, which evaporates in dry air at $T_g = 673$ K. For this test case, we set $Re = 25$, $We = 0.1$, $Pr = Sc = 1$, $\lambda_\rho = 770$, $\lambda_\mu = 202$, $\lambda_k = 20$, $\lambda_{c_p} = 2.1$. Zero-pressure outflow boundary conditions are prescribed (therefore, $p_{th} = p_{th,0}$) and the assumption of constant liquid bulk density is relaxed (see Ni *et al.* 2021, for more details). The whole set of governing equations are solved in a square domain $[-10d_0; 10d_0]^2$ using 256×256 grid points. Once evaporation starts, the liquid droplet undergoes a local initial expansion (i.e., $(d/d_0)^2 > 1$) until $t/d_0^2 \approx 2$, after which the d^2 regime is approached (see figure 19a). Overall, good agreement between our simulations and the reference data is observed, confirming once more the validity of our numerical algorithm.

C.3. *Single droplet evaporating in homogeneous isotropic turbulence*

As a final validation case, we reproduce the experimental results in Verwey & Birouk (2018), reproduced also in Dodd *et al.* (2021), consisting of a single n-heptane droplet
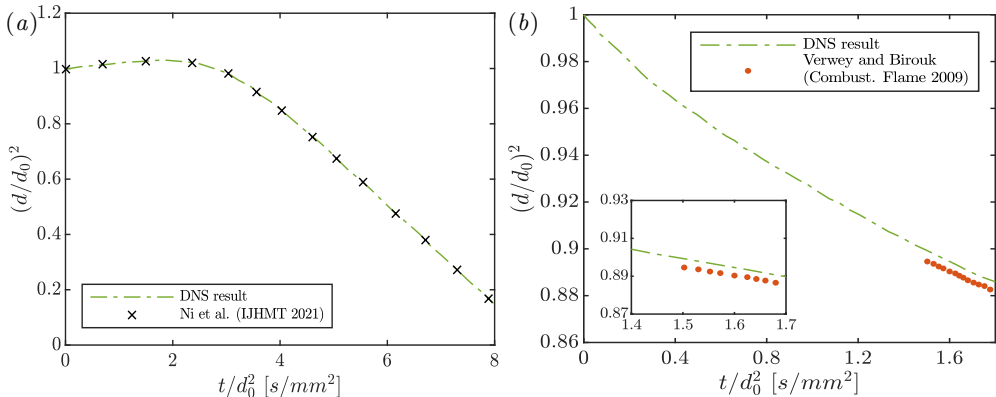
Figure 19: Temporal evolution of the instantaneous droplet diameter $(d/d_0)^2$ over the initial value for the *a*): validation case described in C.2 and the *b*): C.3.

of initial diameter $d_0 = 200 \ \mu m$, which evaporates in nitrogen at $T_g = 348$ K and $p_{th,0} = 10$ bar. For this test case, we consider homogeneous isotropic turbulence sustained by an artificial forcing (Podvigina & Pouquet 1994) at a Reynolds number based on the Taylor's microscale $Re_\lambda = u'_{rms}\lambda/\nu_{g,r} \approx 32$. The initial droplet Weber number $We_{rms} = \rho_{g,r}u'^2_{rms}d_0/\sigma$ is set equal to 0.0044, $Pr = 0.715$, $Sc = 2.81$, $Ste = 1.05$, $\lambda_\rho = 25.27$, $\lambda_\mu = 11.82$, $\lambda_k = 3.72$ and $\lambda_{c_p} = 2.45$. The whole set of governing equations are solved in a cubic domain $[-16d_0; 16d_0]^3$ using 768^3 grid points corresponding to about 48 grid points per initial diameter. Figure 19b reports $(d/d_0)^2$ as a function of t/d_0^2 for the both the experimental and the numerical results. A good agreement is observed with a deviation of evaporation rate K_{DNS} of less then 7 % with respect to the experimental data, which is considered a satisfactory result and within the uncertainty of the measurement (Verwey & Birouk 2018).

Appendix D. Improved Adams-Bashforth scheme for HST simulations

Kasbaoui *et al.* (2017) show that that the classical Adams-Bashforth scheme (AB2) employed in Gerz *et al.* (1989) is not suitable for the direct numerical simulations of homogeneous shear turbulence. Using as a benchmark the Kelvin modes derived in the framework of the Rapid Distorsion Theory (RDT) (Maxey 1982; Isaza & Collins 2009), they show that the method fails to reproduce the analytical solution with an unbounded growth of the error. In this Appendix, we propose a modification of the classical Adams-Bashforth scheme able to reproduce the Kelvin modes and, more generally, stable and accurate simulations.

D.1. *Proof the the numerical stability*

We follow the approach proposed in Kasbaoui *et al.* (2017) and compute the time discretization error introduced by the classical Adams-Bashforth scheme using the following simplified equation

$$\frac{\partial u}{\partial t} + \mathcal{S}z\frac{\partial u}{\partial x} = Au, \qquad (D\,1)$$

where A is a positive constant and $\mathcal{S}$ is the applied shear. As noted in Kasbaoui *et al.* (2017), equation (D 1) allows us to remove the complications due to the pressure

gradient while preserving some important key features of homogeneously sheared flows, i.e. the exponential growth of the turbulent kinetic energy (Maxey 1982). The solution of equation (D 1), $u = \hat{u}(t) \exp(i\mathbf{k} \cdot \mathbf{x})$, needs to satisfy two conditions for the amplitude $\hat{u}(t)$ and for the wave-vector $\mathbf{k}$:

$$\frac{d\hat{u}}{dt} = A\hat{u}, \qquad (D\,2a)$$

$$\frac{d\mathbf{k}}{dt} \cdot \mathbf{x} = -\mathcal{S}z\mathbf{k} \cdot \mathbf{e}_x. \qquad (D\,2b)$$

Assuming that the discretization error evolves as a wave of amplitude $\hat{\varepsilon}$ and wavevector $\mathbf{k}$, at the nth time-step

$$\varepsilon^n = \hat{\varepsilon}^n \exp(i\mathbf{k}^n \cdot \mathbf{x}). \qquad (D\,3)$$

Employing the classical Adams-Bashforth integration scheme, we obtain a first intermediate error neglecting the mean shear contribution,

$$\bar{\varepsilon}^{n+1} = \varepsilon^n + A\Delta t^{n+1} \left[\gamma_1 \mathbf{RU}(\hat{\varepsilon}^n, \mathbf{k}^n) - \gamma_2 \mathbf{RU}(\hat{\varepsilon}^{n-1}, \mathbf{k}^{n-1}) \right], \qquad (D\,4)$$

where $\mathbf{RU}$ represents the discrete operator for the spatial terms in the governing equation of the error and $\gamma_1 = (1 + 0.5\Delta t^{n+1}/\Delta t^n)$ and $\gamma_2 = 0.5\Delta t^{n+1}/\Delta t^n$ are the two coefficients of the Adams-Bashforth scheme for a variable time-step size. Note again that, at this stage, the mean shear contribution is not included in $\mathbf{RU}$.

Following the approach proposed by Gerz *et al.* (1989), we set $\mathbf{RU}(\hat{\varepsilon}^n, \mathbf{k}^n) = \hat{\varepsilon}^n \exp(i\mathbf{k}^n \cdot \mathbf{x})$ and $\mathbf{RU}(\hat{\varepsilon}^{n-1}, \mathbf{k}^{n-1}) = \hat{\varepsilon}^{n-1} \exp(i\mathbf{k}^{n-1} \cdot \mathbf{x})$. Moreover, by using the identity $\exp(i\mathbf{k}^{n-1} \cdot \mathbf{x}) = \exp(-i\Delta\mathbf{k} \cdot \mathbf{x}) \exp(i\mathbf{k}^n \cdot \mathbf{x})$, equation (D 4) becomes:

$$\bar{\varepsilon}^{n+1} = \left\{ \varepsilon^n + A\Delta t^{n+1} \left[\gamma_1 \hat{\varepsilon}^n - \gamma_2 \hat{\varepsilon}^{n-1} \exp(-i\Delta\mathbf{k} \cdot \mathbf{x}) \right] \right\} \exp(i\mathbf{k}^n \cdot \mathbf{x}), \qquad (D\,5)$$

where $\Delta\mathbf{k} = \mathbf{k}^n - \mathbf{k}^{n-1}$. Next, the mean shear contribution is included and this results in an error at time $n + 1$,

$$\varepsilon^{n+1} = \overbrace{\left\{ \varepsilon^n + A\Delta t^{n+1} \left[\gamma_1 \hat{\varepsilon}^n - \gamma_2 \hat{\varepsilon}^{n-1} \exp(-i\Delta\mathbf{k} \cdot (\mathbf{x} - \Delta t^{n+1}\mathcal{S}z\mathbf{e}_x)) \right] \right\}}^{\hat{\varepsilon}^{n+1}} \cdot$$
$$\exp[\underbrace{i\mathbf{k}^n \cdot (\mathbf{x} - \Delta t^{n+1}\mathcal{S}z\mathbf{e}_x)}_{i\mathbf{k}^{n+1}}]. \qquad (D\,6)$$

If we analyze equation (D 6), we see that the new wavevector $\mathbf{k}^{n+1}$ satisfies the first condition, i.e., eqn (D 2a). In fact:

$$\mathbf{k}^n \cdot (\mathbf{x} - \Delta t^{n+1}\mathcal{S}z\mathbf{e}_x) = \mathbf{k}^{n+1} \cdot \mathbf{x} \rightarrow \frac{\mathbf{k}^{n+1} - \mathbf{k}^n}{\Delta t^{n+1}} \cdot \mathbf{x} = -\mathcal{S}z\mathbf{k}^n \cdot \mathbf{e}_x. \qquad (D\,7)$$

Conversely, the amplitude at the new time level, $\hat{\varepsilon}^{n+1}$, does not satisfy the condition (D 2b) since it contains a spatial-dependent term, $\Delta\mathbf{k}$, which is caused by the difference in orientation between the wavevector at the current and old time level, n and $n - 1$.

The approach proposed in this work improves the method by Gerz *et al.* (1989) by removing the spatial dependent term, $\Delta\mathbf{k}$. To this end, the third term on the right hand side of equation (D 4) is first shear-mapped to the current time level:

$$\hat{\varepsilon}^{n-1} \exp(i\mathbf{k}^{n-1} \cdot (\mathbf{x} - \Delta t^n \mathcal{S}z\mathbf{e}_x)) = \hat{\varepsilon}^{n-1} \exp(i\mathbf{k}^n \cdot \mathbf{x}). \qquad (D\,8)$$

Equation (D 8) is key to obtain two wave errors of different amplitudes (i.e., $\hat{\varepsilon}^n$ and $\hat{\varepsilon}^{n-1}$)
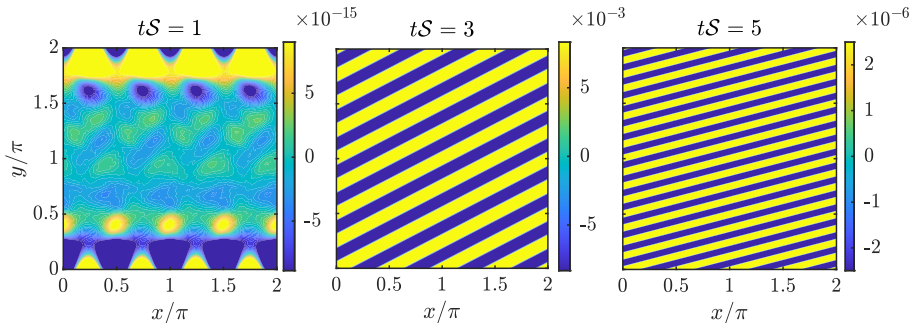
Figure 20: Temporal evolution of the horizontal mode for $t\mathcal{S} = 1$, 3 and 5 using the modified Adams-Bashforth.

but equal wavevector, i.e., $\mathbf{k}^n$. Inserting equation (D 8) in equation (D 4)

$$\bar{\varepsilon}^{n+1} = \left\{ \varepsilon^n + A\Delta t^{n+1} \left[\gamma_1 \hat{\varepsilon}^n - \gamma_2 \hat{\varepsilon}^{n-1} \right] \right\} \exp(i\mathbf{k}^n \cdot \mathbf{x}). \tag{D 9}$$

Next, the shear-mapping step is applied to equation (D 9), providing an error at $n+1$

$$\varepsilon^{n+1} = \overbrace{\left[\varepsilon^n + A\Delta t^{n+1} \left(\gamma_1 \hat{\varepsilon}^n - \gamma_2 \hat{\varepsilon}^{n-1} \right) \right]}^{\hat{\varepsilon}^{n+1}} \exp[\underbrace{i\mathbf{k}^n \cdot (\mathbf{x} - \Delta t^{n+1} \mathcal{S} z \mathbf{e}_x)}_{i\mathbf{k}^{n+1}}]. \tag{D 10}$$

As expected and similarly to what observed for (D 5), equation (D 10) satisfies the condition for $\mathbf{k}^{n+1}$ given by (D 2b). This time, however, also the condition (D 2a) is met since the term $\hat{\varepsilon}^{n+1}$ does not contain any spatial dependent term, i.e., $\mathbf{k}$. The effectiveness of the proposed approach is shown in the next subsection with an analytical benchmark.

D.2. *Validation*

To validate the modified algorithm proposed here, we employ the two-dimensional analytical Kelvin modes derived in the framework of the RDT,

$$v^K(\mathbf{x}, t) = v_0^K \left(\frac{k_0}{k} \right)^2 \exp\left[-\frac{t\mathcal{S}}{Re_\lambda} \left(k_0^2 - k_{x,0} k_{y,0} \mathcal{S} t + \frac{k_{x,0}^2 \mathcal{S}^2 t^2}{3} \right) \right] \exp(i\mathbf{k} \cdot \mathbf{x}),$$

$$u^K(\mathbf{x}, t) = -\frac{k_y(t)}{k_x} v^K(\mathbf{x}, t),$$

$$k_y = k_{y,0} - k_x \mathcal{S} t,$$

where Re_λ, defined as $\mathcal{S}\lambda_0^2/\nu$, is the Reynolds number based on the perturbation wavelength $\lambda_0 = \sqrt{(2\pi/k_x)^2 + (2\pi/k_{y,0})^2}$, taken as a reference length. As done by Kasbaoui *et al.* (2017), we consider a two-dimensional square box $l_x = l_y = 2\pi$, discretized with $N = 128$ points along each direction. The analytical solution (D 11) is employed as initial condition, with initial vertical amplitude $v_0^K = \sqrt{2}/2$, initial wavevector $\mathbf{k}_0 = (4, 1)$ and $Re_\lambda = 208$. We compare three time-integration methods: (1) the Adams-Bashforth (AB2) in the two variants (classical and modified), (2) the Third-order Runge-Kutta (RK3) method proposed in Tanaka (2017); Yousefi *et al.* (2020) and (3) the Explicit Crank-Nicholson (CN2), proposed in Kasbaoui *et al.* (2017). In all cases, the momentum equation is advanced with a constant time step, $\Delta t = 0.25 (\mathcal{S}N)^{-1}$. Figures 20–22 report the horizontal mode obtained with the three different time-integration schemes, which according to the RDT should go to zero at $t\mathcal{S} = 1$. Using the modified AB2 scheme and
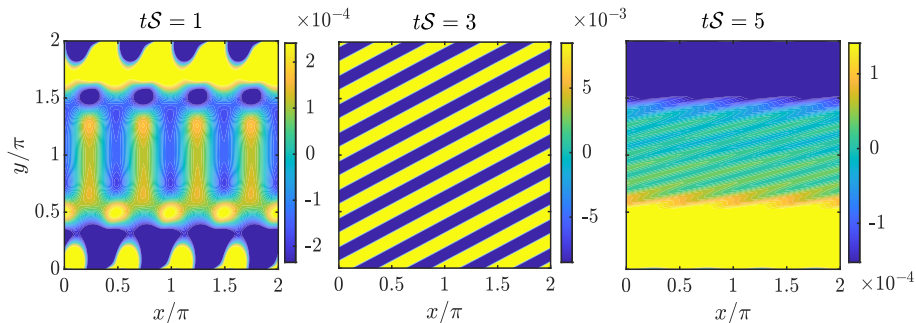
Figure 21: Temporal evolution of the horizontal mode for $t\mathcal{S} = 1$, 3 and 5 using the standard Adams-Bashforth.
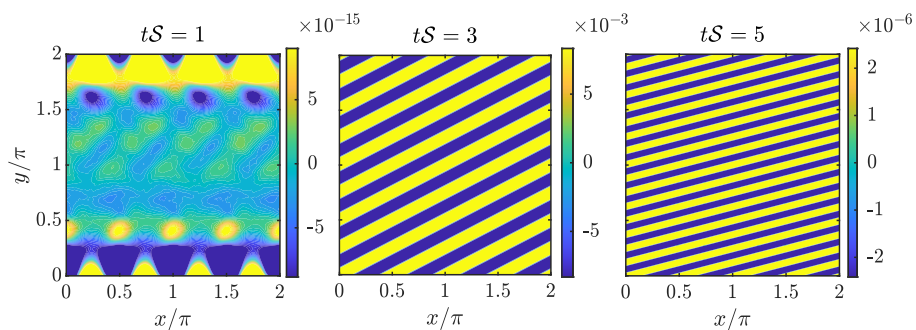

Figure 22: Temporal evolution of the horizontal mode for $t\mathcal{S} = 1$, 3 and 5 using the explicit Crank-Nicolson method.
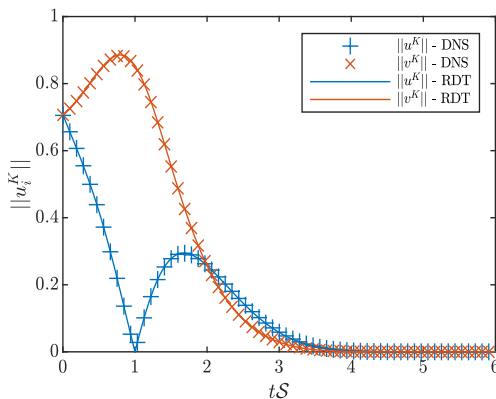

Figure 23: Comparison between the numerical solution obtained with AB2 (proposed method) and the analytical results from RDT.

CN2, we obtain almost identical results and zero horizontal mode up to machine precision at $t\mathcal{S} = 1$. Conversely, using the original approach by Gerz (figure 21), the normal mode does not go to zero for $t\mathcal{S} = 1$ and for $t\mathcal{S} = 5$ the numerical errors largely affect the solution.

The excellent agreement between the results obtained with our approach and the analytical solution from RDT are reported in figure 23. A more detailed analysis considers
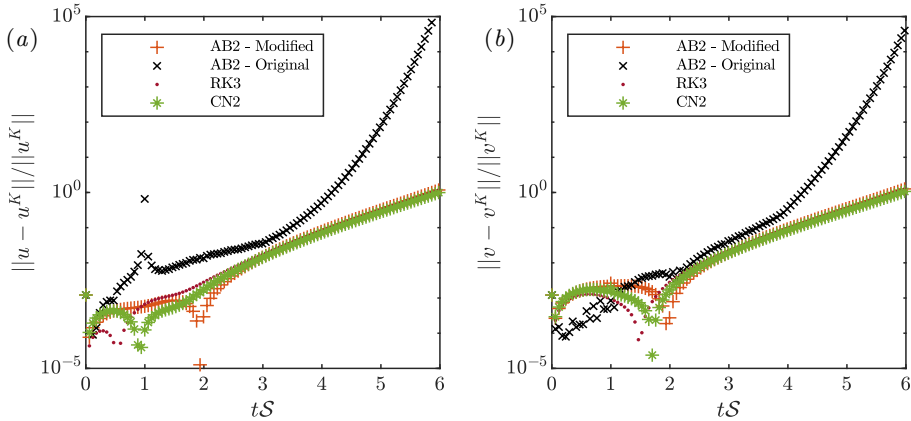
Figure 24: Temporal evolution of the discretization of error (in log scale) for: (a) the horizontal mode (i.e., u), (b): the vertical mode (i.e., v) using the three time integration methods, AB2 - Gerz et al. and AB2 - Modified, RK3 and CN2.

the evolution in time of the relative error, reported in figure 24 for the horizontal and vertical Kelvin modes. The modified AB2, RK3 and CN2 provide similar errors, especially for $t\mathcal{S} > 2$, while for $t\mathcal{S} \leqslant 2$, the CN2 method appears to be slightly more accurate. On the contrary, the error of the classical AB2 is well above that from the other three methods, with a local peak at $t\mathcal{S} = 1$ in the horizontal mode u^K, as already observed in the first panel of figure 21. Further, the error evolves at a much faster pace, which is the main reason for the poor performance of the classic AB2 in more demanding simulations.

REFERENCES

ABRAMZON, B & SIRIGNANO, WA 1989 Droplet vaporization model for spray combustion calculations. *International journal of heat and mass transfer* **32** (9), 1605–1618.

ALBERNAZ, DANIEL L, DO-QUANG, MINH, HERMANSON, JIM C & AMBERG, GUSTAV 2017 Droplet deformation and heat transfer in isotropic turbulence. *Journal of Fluid Mechanics* **820**, 61–85.

BALACHANDAR, S, ZALESKI, STEPHANE, SOLDATI, ALFREDO, AHMADI, GOODARZ & BOUROUIBA, LYDIA 2020 Host-to-host airborne transmission as a multiphase flow problem for science-based social distance guidelines.

BIROUK, MADJID & GÖKALP, ISKENDER 2006 Current status of droplet evaporation in turbulent flows. *Progress in Energy and Combustion Science* **32** (4), 408–423.

BOUROUIBA, LYDIA 2020 Turbulent gas clouds and respiratory pathogen emissions: potential implications for reducing transmission of covid-19. *Jama* **323** (18), 1837–1838.

BOUROUIBA, LYDIA 2021 The fluid dynamics of disease transmission. *Annual Review of Fluid Mechanics* **53**, 473–508.

BUKHVOSTOVA, A, RUSSO, E, KUERTEN, JOHANNES GM & GEURTS, BERNARDUS J 2014 Comparison of dns of compressible and incompressible turbulent droplet-laden heated channel flow with phase transition. *International journal of multiphase flow* **63**, 68–81.

CHONG, KAI LEONG, NG, CHONG SHEN, HORI, NAOKI, YANG, RUI, VERZICCO, ROBERTO & LOHSE, DETLEF 2021 Extended lifetime of respiratory droplets in a turbulent vapor puff and its implications on airborne disease transmission. *Physical review letters* **126** (3), 034502.

COSTA, PEDRO 2018 A fft-based finite-difference solver for massively-parallel direct numerical simulations of turbulent flows. *Computers & Mathematics with Applications* **76** (8), 1853–1862.

DALLA BARBA, FEDERICO, SCAPIN, NICOLÓ, DEMOU, ANDREAS D, ROSTI, MARCO E, PICANO,

FRANCESCO & BRANDT, LUCA 2020 An interface capturing method for liquid-gas flows at low-mach number. *Computers & Fluids* p. 104789.

DAUXOIS, THIERRY, PEACOCK, THOMAS, BAUER, PETER, CAULFIELD, COLM-CILLE P, CENEDESE, CLAUDIA, GORLÉ, CATHERINE, HALLER, GEORGE, IVEY, GREG N, LINDEN, PAUL F, MEIBURG, ECKART & OTHERS 2021 Confronting grand challenges in environmental fluid mechanics. *Physical Review Fluids* **6** (2), 020501.

DE RIVAS, A & VILLERMAUX, E 2016 Dense spray evaporation as a mixing process. *Physical Review Fluids* **1** (1), 014201.

DEMOU, AD, FRANTZIS, C & GRIGORIADIS, DGE 2019 A low-mach methodology for efficient direct numerical simulations of variable property thermally driven flows. *International Journal of Heat and Mass Transfer* **132**, 539–549.

DODD, MICHAEL S & FERRANTE, ANTONINO 2014 A fast pressure-correction method for incompressible two-fluid flows. *Journal of Computational Physics* **273**, 416–434.

DODD, MICHAEL S, MOHADDES, DANYAL, FERRANTE, ANTONINO & IHME, MATTHIAS 2021 Analysis of droplet evaporation in isotropic turbulence through droplet-resolved dns. *International Journal of Heat and Mass Transfer* **172**, 121157.

ELGHOBASHI, SAID 2019 Direct numerical simulation of turbulent flows laden with droplets or bubbles. *Annual Review of Fluid Mechanics* **51**, 217–244.

GERZ, THOMAS, SCHUMANN, ULRICH & ELGHOBASHI, SE 1989 Direct numerical simulation of stratified homogeneous turbulent shear flows. *Journal of Fluid Mechanics* **200**, 563–594.

GÖKALP, ISKENDER, CHAUVEAU, CHRISTIAN, SIMON, OLIVIER & CHESNEAU, XAVIER 1992 Mass transfer from liquid fuel droplets in turbulent flow. *Combustion and flame* **89** (3-4), 286–298.

HUBBARD, GL, DENNY, VE & MILLS, AF 1975 Droplet evaporation: effects of transients and variable properties. *International journal of heat and mass transfer* **18** (9), 1003–1008.

II, SATOSHI, SUGIYAMA, KAZUYASU, TAKEUCHI, SHINTARO, TAKAGI, SHU, MATSUMOTO, YOICHIRO & XIAO, FENG 2012 An interface capturing method with a continuous function: The thinc method with multi-dimensional reconstruction. *Journal of Computational Physics* **231** (5), 2328–2358.

ISAZA, JUAN C & COLLINS, LANCE R 2009 On the asymptotic behaviour of large-scale turbulence in homogeneous shear flow. *Journal of fluid mechanics* **637**, 213.

KASBAOUI, M HOUSSEM, PATEL, RAVI G, KOCH, DONALD L & DESJARDINS, OLIVIER 2017 An algorithm for solving the navier–stokes equations with shear-periodic boundary conditions and its application to homogeneously sheared turbulence. *Journal of Fluid Mechanics* **833**, 687–716.

KUERTEN, JOHANNES GM 2016 Point-particle dns and les of particle-laden turbulent flow-a state-of-the-art review. *Flow, turbulence and combustion* **97** (3), 689–713.

LANGMUIR, IRVING 1918 The evaporation of small spheres. *Physical review* **12** (5), 368.

LEONARD, BRIAN P 1979 A stable and accurate convective modelling procedure based on quadratic upstream interpolation. *Computer methods in applied mechanics and engineering* **19** (1), 59–98.

LUPO, GIANDOMENICO, ARDEKANI, MEHDI NIAZI, BRANDT, LUCA & DUWIG, CHRISTOPHE 2019 An immersed boundary method for flows with evaporating droplets. *International Journal of Heat and Mass Transfer* **143**, 118563.

LUPO, GIANDOMENICO & DUWIG, CHRISTOPHE 2020 Uncertainty quantification of multispecies droplet evaporation models. *International Journal of Heat and Mass Transfer* **154**, 119697.

LUPO, GIANDOMENICO, GRUBER, ANDREA, BRANDT, LUCA & DUWIG, CHRISTOPHE 2020 Direct numerical simulation of spray droplet evaporation in hot turbulent channel flow. *International Journal of Heat and Mass Transfer* **160**, 120184.

MAJDA, ANDREW & SETHIAN, JAMES 1985 The derivation and numerical solution of the equations for zero mach number combustion. *Combustion science and technology* **42** (3-4), 185–205.

MANDAL, DEEPAK KUMAR & BAKSHI, SHAMIT 2012 Internal circulation in a single droplet evaporating in a closed chamber. *International journal of multiphase flow* **42**, 42–51.

MARTI, FERRAN, MARTINEZ, OSCAR, MAZO, DAVID, GARMAN, JOHN & DUNN-RANKIN, DEREK

2017 Evaporation of a droplet larger than the kolmogorov length scale immersed in a relative mean flow. *International Journal of Multiphase Flow* **88**, 63–68.

MASHAYEK, FARZAD 1998a Direct numerical simulations of evaporating droplet dispersion in forced low mach number turbulence. *International journal of heat and mass transfer* **41** (17), 2601–2617.

MASHAYEK, FARZAD 1998b Droplet–turbulence interactions in low-mach-number homogeneous shear two-phase flows. *Journal of Fluid Mechanics* **367**, 163–203.

MAXEY, MR 1982 Distortion of turbulence in flows with parallel streamlines. *Journal of Fluid Mechanics* **124**, 261–282.

MAXEY, MARTIN 2017 Simulation methods for particulate flows and concentrated suspensions. *Annual Review of Fluid Mechanics* **49**, 171–193.

MÉÈS, L, GROSJEAN, N, MARIÉ, JEAN-LOUIS & FOURNIER, C 2020 Statistical lagrangian evaporation rate of droplets released in a homogeneous quasi-isotropic turbulence. *Physical Review Fluids* **5** (11), 113602.

MITTAL, RAJAT, NI, RUI & SEO, JUNG-HEE 2020 The flow physics of covid-19. *Journal of fluid Mechanics* **894**.

MOTHEAU, EMMANUEL & ABRAHAM, JOHN 2016 A high-order numerical algorithm for dns of low-mach-number reactive flows with detailed chemistry and quasi-spectral accuracy. *Journal of Computational Physics* **313**, 430–454.

NG, CHONG SHEN, CHONG, KAI LEONG, YANG, RUI, LI, MOGENG, VERZICCO, ROBERTO & LOHSE, DETLEF 2021 Growth of respiratory droplets in cold and humid air. *Physical Review Fluids* **6** (5), 054303.

NI, ZHAOJING, HESPEL, CAMILLE, HAN, KAI & FOUCHER, FABRICE 2021 Numerical simulation of heat and mass transient behavior of single hexadecane droplet under forced convective conditions. *International Journal of Heat and Mass Transfer* **167**, 120736.

PIEDRA, S, LU, J, RAMOS, E & TRYGGVASON, G 2015 Numerical study of the flow and heat transfer of bubbly flows in inclined channels. *International Journal of Heat and Fluid Flow* **56**, 43–50.

PINHEIRO, ABGAIL P, VEDOVOTO, JOÃO MARCELO, DA SILVEIRA NETO, ARISTEU & VAN WACHEM, BEREND GM 2019 Ethanol droplet evaporation: effects of ambient temperature, pressure and fuel vapor concentration. *International Journal of Heat and Mass Transfer* **143**, 118472.

PODVIGINA, O & POUQUET, A 1994 On the non-linear stability of the 1: 1: 1 abc flow. *Physica D: Nonlinear Phenomena* **75** (4), 471–508.

PUMIR, ALAIN 1996 Turbulence in homogeneous shear flows. *Physics of Fluids* **8** (11), 3112–3127.

RANZ, WE, MARSHALL, W R_ & OTHERS 1952 Evaporation from drops. *Chem. eng. prog* **48** (3), 141–146.

REID, ROBERT C, PRAUSNITZ, JOHN M & POLING, BRUCE E 1987 The properties of gases and liquids .

REVEILLON, JULIEN & DEMOULIN, FRANÇOIS-XAVIER 2007 Effects of the preferential segregation of droplets on evaporation and turbulent mixing. *Journal of Fluid Mechanics* **583**, 273–302.

ROSTI, ME, CAVAIOLA, M, OLIVIERI, S, SEMINARA, A & MAZZINO, A 2021 Turbulence role in the fate of virus-containing droplets in violent expiratory events. *Physical Review Research* **3** (1), 013091.

ROSTI, ME, OLIVIERI, S, CAVAIOLA, M, SEMINARA, A & MAZZINO, A 2020 Fluid dynamics of covid-19 airborne infection suggests urgent data for a scientific design of social distancing. *Scientific reports* **10** (1), 1–9.

ROSTI, MARCO E, DE VITA, FRANCESCO & BRANDT, LUCA 2019a Numerical simulations of emulsions in shear flows. *Acta Mechanica* **230** (2), 667–682.

ROSTI, MARCO E, GE, ZHOUYANG, JAIN, SUHAS S, DODD, MICHAEL S & BRANDT, LUCA 2019b Droplets in homogeneous shear turbulence. *Journal of Fluid Mechanics* **876**, 962–984.

RUSSO, E, KUERTEN, JOHANNES GM, VAN DER GELD, CWM & GEURTS, BERNARDUS J 2014 Water droplet condensation and evaporation in turbulent channel flow. *Journal of fluid mechanics* **749**, 666–700.

SÁENZ, PJ, WRAY, AW, CHE, Z, MATAR, OK, VALLURI, P, KIM, J & SEFIANE, K 2017

Dynamics and universal scaling law in geometrically-controlled sessile drop evaporation. *Nature communications* **8** (1), 1–9.

SAHU, S, HARDALUPAS, Y & TAYLOR, AMKP 2018 Interaction of droplet dispersion and evaporation in a polydispersed spray. *Journal of Fluid Mechanics* **846**, 37–81.

SCAPIN, NICOLÒ, COSTA, PEDRO & BRANDT, LUCA 2020 A volume-of-fluid method for interface-resolved simulations of phase-changing two-fluid flows. *Journal of Computational Physics* **407**, 109251.

SEKIMOTO, ATSUSHI, DONG, SIWEI & JIMÉNEZ, JAVIER 2016 Direct numerical simulation of statistically stationary and homogeneous shear turbulence and its relation to other shear flows. *Physics of Fluids* **28** (3), 035101.

SPAN, ROLAND & WAGNER, WOLFGANG 1996 A new equation of state for carbon dioxide covering the fluid region from the triple-point temperature to 1100 k at pressures up to 800 mpa. *Journal of physical and chemical reference data* **25** (6), 1509–1596.

TANAKA, MITSURU 2017 Effect of gravity on the development of homogeneous shear turbulence laden with finite-size particles. *Journal of Turbulence* **18**, 1–36.

TONINI, SIMONA & COSSALI, GE 2013 An exact solution of the mass transport equations for spheroidal evaporating drops. *International Journal of Heat and Mass Transfer* **60**, 236–240.

VERWEY, CAMERON & BIROUK, MADJID 2018 Fuel vaporization: Effect of droplet size and turbulence at elevated temperature and pressure. *Combustion and Flame* **189**, 33–45.

VERWEY, CAMERON & BIROUK, MADJID 2020 Experimental investigation of the evaporation of suspended mono-sized heptane droplets in turbulence intensities approaching unity. *Combustion and Flame* **219**, 425–436.

VILLERMAUX, EMMANUEL, MOUTTE, ALEXANDRE, AMIELH, MURIEL & MEUNIER, PATRICE 2017 Fine structure of the vapor field in evaporating dense sprays. *Physical Review Fluids* **2** (7), 074501.

WANG, JIETUO, DALLA BARBA, FEDERICO & PICANO, FRANCESCO 2021 Direct numerical simulation of an evaporating turbulent diluted jet-spray at moderate reynolds number. *International Journal of Multiphase Flow* **137**, 103567.

WANG, YANXING, CHEN, XIAODONG, WANG, XINGJIAN & YANG, VIGOR 2019 Vaporization of liquid droplet with large deformation and high mass transfer rate, ii: Variable-density, variable-property case. *Journal of Computational Physics* **394**, 1–17.

WEISS, PHILIPP, GIDDEY, VALENTIN, MEYER, DANIEL W & JENNY, PATRICK 2020 Evaporating droplets in shear turbulence. *Physics of Fluids* **32** (7), 073305.

WEISS, PHILIPP, MEYER, DANIEL W & JENNY, PATRICK 2018 Evaporating droplets in turbulence studied with statistically stationary homogeneous direct numerical simulation. *Physics of Fluids* **30** (8), 083304.

WONG, SHWIN-CHUNG & LIN, AR-CHENG 1992 Internal temperature distributions of droplets vaporizing in high-temperature convective flows. *Journal of fluid mechanics* **237**, 671–687.

YOUSEFI, ALI, ARDEKANI, MEHDI NIAZI & BRANDT, LUCA 2020 Modulation of turbulence by finite-size particles in statistically steady-state homogeneous shear turbulence. *Journal of Fluid Mechanics* **899**.